Università degli Studi di Napoli "Federico II"

Scuola Politecnica e delle Scienze di Base
Area Didattica di Scienze Matematiche Fisiche e Naturali

Dipartimento di Fisica

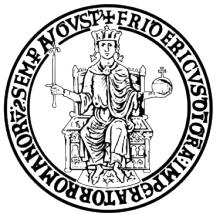

Laurea Magistrale in Fisica

Selection of charged current muon anti-neutrino interactions in the near detector of the T2K experiment with an improved acceptance

Relatori:
Prof. Vittorio Palladino
Dott.ssa Gianfranca de Rosa
Dott. Ciro Riccio

Candidato:
Lorenzo Di Colandrea
Matricola N94/226

Anno Accademico 2017-2018

Contents

List of Figures

List of Tables

Introduction

The T2K (Tokai-to-Kamioka) experiment is a long baseline neutrino oscillation experiment that uses an intense proton beam generated by the J-PARC accelerator in Tokai, Japan. The main focus of the experiment is to measure neutrino flavour oscillations observing ν_e appearance in a ν_μ beam. In addition, the Collaboration aims to measure neutrino cross-sections, CP violation and sterile neutrino searches. The experiment neutrino beam travels toward the far detector, Super-Kamiokande, located in the Mozumi mine, 295 km far from the neutrino production point. At 280 m proton beam target, there is a near detector complex which consists of detectors: INGRID and ND280. The near detector ND280 consists of:

- the PØD and TPC/FGD sandwich (tracker), both of which are placed inside of a metal frame container, called the "basket".
- An electromagnetic calorimeter (ECAL) that surrounds the basket.
- The UA1 magnet instrumented with scintillator as a muon range detector(SMRD)

The near detector complex is used to measure the unoscillated flux and neutrino cross-sections in water and carbon. After the discovery of the electron neutrino appearance, excluding $\theta_{13} = 0$ with a significance of 7.3σ, T2K began collecting data in anti-neutrino mode to search for anti-neutrino oscillation. The analysis of neutrino and anti-neutrino charged current interactions in the near detector ND280 is fundamental to the reduction of the flux prediction and cross-section modelling systematic uncertainties in the oscillation analysis. ND280 data also gives us the opportunity to measure anti-neutrino cross-sections at the energy around 600 MeV.

The goal of this thesis work is to realize a selection of $\bar{\nu}_\mu$ charged current interactions in ND280 with an improved acceptance. The previous selection required that an event be accepted only if the positive muon candidate track had more 18 hits within the TPC following the reference FGD. The writing of this thesis is structured as follow:

- **Chapter 1**: an introduction to neutrino oscillation physics is given to put in context the work;
- **Chapter 2**: the T2K set up is presented in detail and give some important results achieved by the Collaboration;

- **Chapter 3**: a synthetic review of the neutrino interaction with matter is given to understand better which neutrino interactions are significant for the T2K experiment;
- **Chapter 4**: show the $\bar{\nu}_\mu$ charged current selection in detail.

Chapter 1

Neutrino physics

1.1 Discovery of neutrino

The first neutrino hypothesis is linked to the study of β-decay. Unlike what had been seen for discrete emitted spectrum in α and γ-decay, J. Chadwick discovered a continuous energy spectrum of electrons emitted in β-decay. To explain this observation W. Pauli, in a letter dated 4 December 1930 to a group of physicists in a Tübingen meeting, proposed that β-decay was a three body decay like:

$$M(A, Z) \rightarrow D(A, Z-1) + e^{+} + \nu \tag{1.1}$$

where M(A,Z) is the mother nucleus and D(A,Z-1) its daughter. The third particle emitted in decay was a new undetectable particle, later called "neutrino" by Enrico Fermi, carrying away energy and spin. In this hypothesis that neutrinos interact only weakly with matter, have no charge and spin $\frac{1}{2}$ for angular momentum conservation. Moreover the electron spectrum was found to have maximum energy compatible with the kinematic upper limit resulting from the assumption that the mass of the neutrino was exactly zero. β-decay also exists with emission of an electron and in that case the antiparticle of the neutrino is assumed to be emitted.

In the mid 1950's, L. Cowan and F. Reines designed the experiment to verify the existence of the neutrino. Following an idea of Bruno Pontecorvo, nuclear reactors were used as source, expected to produce neutrino fluxes on the order of $10^2 - 10^3$ neutrinos per second per cm^2, far higher than the flux attainable from any other radioactive sources. The basic detection reaction was

$$\bar{\nu}_e + p \rightarrow e^{+} + n \tag{1.2}$$

The coincidence of the two 511 keV gammas produced by the positron annihilation and the gamma produced by neutron capture gives a unique signature of an anti-neutrino interaction. Cowan and Reines used a water tank (Figure 1.1) with dissolved $CdCl_2$ surrounded by two liquid scintillators to detect the coincidence of the three photons.

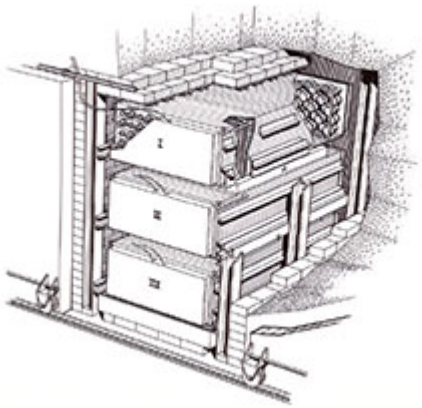

Figure 1.1: Design of Cowan and Reines experiment for neutrino discovery.

1.1.1 The second and third neutrino

In 1958, Bruno Pontecorvo suggested to investigate if the neutrino emitted in β-decay is the same emitted in pion decay.

$$\pi^{\pm} \rightarrow \mu^{\pm} + (\nu/\bar{\nu}) \tag{1.3}$$

The hypothesis was that if only one neutrino exists then interactions of neutrinos produced in pion decays with protons or neutrons should produce as many electrons as muons; on the contrary, if two types of neutrino exist then there is no reason to expect any electrons. The reaction they considered were the following:

$$\nu + n \rightarrow p + e^{-} \tag{1.4}$$

$$\bar{\nu} + p \rightarrow n + e^{+} \tag{1.5}$$

$$\nu + n \rightarrow p + \mu^{-} \tag{1.6}$$

$$\bar{\nu} + p \rightarrow n + \mu^{+} \tag{1.7}$$

In order to answer this question, Mel Schwarz proposed to use a proton accelerator to produce a high energy neutrino beam from the pions decays, because pions can be generated by colliding of high energy protons on a static target. Lederman, Schwartz and Steinberg made their experiment by exposing a detector at the brand-new Alternating Gradient Synchrotron(AGS), the most powerful accelerator in the world, capable of producing the beam needed. The experiment used a beam of the AGS's energetic protons to produce a shower of π mesons, which traveled toward a 5,000-ton steel wall. On the way, they decayed into muons and neutrinos, but only the latter particles could pass

through the wall. A spark chamber was used to detect neutrinos. There, the impact of neutrinos on aluminium plates produced muon spark trails that could be detected and photographed, proving the existence of muon-neutrinos.

In 1974 was discovered a third type of lepton (τ), so the existence of another type of neutrino became necessary for the theory of the weak interaction that had already been developed years before. The discovery of ν_τ was announced in July 2000 by the DONuT(*Direct Obsevation of the Nu Tau*) collaboration at Fermilab [27]. In the DONuT experiment a proton beam, accelerated by the Tevatron, was used to produce a tau neutrino beam from decay of charmed mesons. Then the neutrino beam passed through several sheets of nuclear emulsion, where a small number of τ neutrino would interact producing a typical track with a "kick" after a few millimetres, indicating the decay of lepton τ.

1.2 Neutrino in the Standard Model

The Standard Model (SM) describes the strong, weak and electromagnetic interactions between elementary particles. It is a gauge theory based on the local symmetry group $SU(3)_C \times SU(2)_L \times U(1)_Y$, where C, L and Y respectively stand for color, left-handed chirality and weak hypercharge. In the SM the particles are classified in two types: fermions and gauge bosons. Fermions are particles of spin 1/2 and each of them has an anti-particle with the same mass but opposite quantum numbers. They are divided in two families: quarks and leptons. Leptons do not interact via strong interactions contrary to quarks. Instead gauge bosons are particles of integer spin and they are able to mediate the interactions. The actual classification of elementary particles is shown in Figure 1.2.

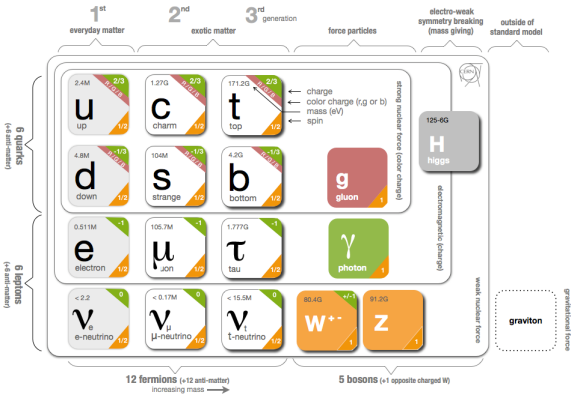

Figure 1.2: Classification of elementary particles in the Standard Model.

Neutrinos are leptons with no charge and only interact through weak interaction. They have been discovered as flavour eigenstates of the interactions by identifying the charged lepton in final state and all observations show that neutrino is left-handed(LH) and anti-neutrino is right-handed(RH). The simplest way to describe this situation is that the neutrinos have exactly mass equal zero: $m_\nu = 0$ in SM.

In the last 20 years, however, the growing experimental evidence of neutrino oscillation has disproved this assumption. The possibility of neutrino oscillation exists if neutrinos are massive and their mass is not the same for all. The mixing originates from the fact that mass eigenstates are different from flavour eigenstates so it is possible to observe $\nu_\alpha \leftrightarrow \nu_\beta$. Each mass eigenstate (ν_1, ν_2, ν_3) propagates as a coherent linear superposition of the flavour eigenstate $(\nu_e, \nu_\mu, \nu_\tau)$ resulting in the possibility of detection of different flavour with probability function of distance.
The neutrino oscillation theory, as we will see in the next section, is governed by the differences of the squared neutrinos masses (Δm^2_{ij} with $i, j = 1, 2, 3$) and not by the individual masses. In this case we can have two different type of mass spectrum depending on the order relation between the 3 neutrinos masses. The existing data do not allow to determine the sign of $\Delta m^2_{31(32)}$ but considering the widely used conventions of numbering the neutrinos with definite mass in two cases, we can write two types of mass spectrum[30]:

- spectrum with Normal Ordering(NO):

$$\begin{aligned} m_1 < m_2 < m_3;\ \Delta m^2_{31} = \Delta m^2_A > 0 \\ \Delta m^2_{21} \equiv \Delta m^2_\odot > 0; \end{aligned} \tag{1.8}$$

- spectrum with Inverting Ordering(IO):

$$\begin{aligned} m_3 < m_1 < m_2; \Delta m^2_{32} = \Delta m^2_A < 0; \\ \Delta m^2_{21} \equiv \Delta m^2_\odot > 0 \end{aligned} \tag{1.9}$$

The determination of the neutrino mass spectrum is known as "determination of neutrino mass ordering" or "determination of neutrino mass hierarchy".

1.2.1 Dirac and Majorana Neutrinos

In order to extend the Standard Model and to make neutrinos massive, two different approaches can be considered. The first gives mass to neutrino via standard Higgs mechanism but in this approach it is difficult to explain why neutrinos have masses so much smaller then the other particles in Standard Model. This neutrino is called Dirac neutrino and like any Dirac particle it is distinct from its antiparticle. The second hypothesis assumes that the neutrino is different (Majorana) type of fermion, that is then the only fermion identical to its own antiparticle. This representation gives rise to RH neutrinos

with very large mass via a new mechanism (the Seesaw Mechanism) that manages to explain the smallness of the neutrino mass eigenstates.

1.3 Phenomenology of the neutrino oscillation

The neutrino oscillation is possible only if neutrinos are massive and different neutrinos have different mass, so the importance of the study of this phenomenon is fundamental in particle physics. The experimental evidence of this phenomenon was found in the 1968 by the Homestake experiment but it remained controversial until Super-Kamiokande and SNO results were published in 1998 and 2002, respectively. In this section we will show that, from a theoretical point of view, neutrino oscillation is described by a neutrino mixing matrix with six free parameters: three mixing angles, a CP violating phase (δ_{CP}) and two independent differences of the squared neutrino masses Δm^2.

The first hypothesis of neutrino oscillation was suggested by Bruno Pontecorvo in 1957 in which he conjectured a $\nu \longleftrightarrow \bar{\nu}$ oscillation, at that time the second neutrino family had not yet been discovered. The oscillation phenomenon was linked to idea that the neutrino was created or destroyed in flavour eigenstates but their evolution was described by mass eigenstates. Flavour transitions have been first considered by Z. Maki, M. Nagakawa and S. Sakata after the discovery of a second type of neutrino, different from ν_e at the Brookhaven AGS in 1962 [30].

1.3.1 Neutrino oscillation in vacuum

The theory is based on quantum mechanical principles. The flavour states $|\nu_\alpha\rangle$ are linear superposition of the mass states $|\nu_k\rangle$:

$$|\nu_\alpha\rangle = \sum_k U_{\alpha k} |\nu_k\rangle \tag{1.10}$$

while the adjoin of this relations is:

$$|\nu_k\rangle = \sum_\alpha U^*_{\alpha k} |\nu_\alpha\rangle \tag{1.11}$$

where $\alpha = e, \mu, \tau$ and $k = 1, 2, 3$. U is the unitary mixing matrix and $|\nu_k\rangle$ are the mass eigenstates with eigenvalues m_k. We assume that a neutrino ν_α, with energy E_k, is created at time $t = 0$ and it propagates along the x direction of a coordinate reference system with the origin where the neutrino is generated. At the beginning the state of neutrino is an eigenstate of weak interaction and, as we have previously seen, it is possible to write the state of neutrino as a superposition of the mass eigenstates that evolves over time as:

$$|\nu_k(x,t)\rangle = e^{-iE_k t} |\nu_k(x,0)\rangle \tag{1.12}$$

where

$$|\nu_k(x,0)\rangle = e^{-ipx}\,|\nu_k\rangle \tag{1.13}$$

with p the momentum of the neutrino, so:

$$|\nu(x,t)\rangle = \sum_k U_{\alpha k} e^{-iE_k t}\,|\nu_k\rangle = \sum_{k,\beta} U_{\alpha k} U^*_{\beta k} e^{ipx} e^{-iE_k t}\,|\nu_\beta\rangle \tag{1.14}$$

At time $t \neq 0$ the neutrino is not in a definite flavour eigenstate but it is a superposition of all weak interaction eigenstates. The time-dependent transition amplitude for a flavour conversion $\nu_\alpha \to \nu_\beta$ is then given by:

$$A(\alpha \to \beta)(t) = \langle \nu_\beta, \nu(x,t)\rangle = \sum_k U^*_{\beta k} U_{\alpha k} e^{ipx} e^{-iE_k t} \tag{1.15}$$

Since the neutrino is relativistic, we can write:

$$E_k = \sqrt{m_k^2 + p_k^2} \cong p_k + \frac{m_k^2}{2p_k} \tag{1.16}$$

for $p_k \gg m_k$ and $E_k \cong p_k$.

$$A(\alpha \to \beta)(t) = \sum_k U^*_{\beta k} U_{\alpha k} e^{-i\frac{m_k^2 L}{2E}} = A(\alpha \to \beta)(L) \tag{1.17}$$

with $L = x = t$ (in natural units) being the distance between source and detector. The neutrino probability P can be obtained from the transition amplitude A:

$$\begin{aligned} P(\alpha \to \beta)(t) = |A(\alpha \to \beta)|^2 = \sum_k \sum_l U_{\alpha k} U^*_{\alpha l} U^*_{\beta k} U_{\beta l} e^{-i(E_k - E_l)t} = \\ \sum_k |U_{\alpha k} U^*_{\beta k}|^2 + 2Re \sum_{l>k} U_{\alpha k} U^*_{\alpha l} U^*_{\beta k} U_{\beta l} e^{-i\frac{\Delta m^2_{kl} L}{2E}} \end{aligned} \tag{1.18}$$

Assuming CP invariance ($U_{\alpha k}$ real), this can be simplified to

$$\begin{aligned} P(\alpha \to \beta)(t) &= \sum_k U^2_{\alpha k} U^2_{\beta k} + 2 \sum_{l>k} U_{\alpha k} U_{\alpha l} U_{\beta k} U_{\beta l} \cos\left(\frac{\Delta m^2_{kl} L}{2E}\right) \\ &= \delta_{\alpha\beta} - 4 \sum_{l>k} U_{\alpha k} U_{\alpha l} U_{\beta k} U_{\beta l} \sin^2\left(\frac{\Delta m^2_{kl} L}{4E}\right) \end{aligned} \tag{1.19}$$

The survival probability of finding the original flavour is

$$P(\alpha \to \alpha) = 1 - \sum_{\alpha \neq \beta} P(\alpha \to \beta) \tag{1.20}$$

As can be seen from 1.19 there will be oscillatory behaviour with distance L as long as there is at least one non zero mass difference and there is a mixing (non-diagonal

terms in U) among the flavours. The observation of oscillations allows no absolute mass measurement, as oscillations are only sensitive to Δm^2. Another feature is the dependence of oscillation probability on the ratio $\frac{L}{E}$. The matrix U can be written as a product of 3 matrices

$$U = \begin{pmatrix} 1 & 0 & 0 \\ 0 & c_{23} & s_{23} \\ 0 & -s_{23} & c_{23} \end{pmatrix} \begin{pmatrix} c_{13} & 0 & s_{13}e^{-i\delta_{CP}} \\ 0 & 1 & 0 \\ -s_{13}e^{i\delta_{CP}} & 0 & c_{13} \end{pmatrix} \begin{pmatrix} c_{12} & s_{12} & 0 \\ -s_{12} & c_{12} & 0 \\ 0 & 0 & 1 \end{pmatrix} \tag{1.21}$$

where $c_{ij} = \cos\theta_{ij}$, $s_{ij} = \sin\theta_{ij}$. The name of this matrix is the *Pontecorvo-Maki-Nakagawa-Sakata matrix*(PMNS). The parameters describing the mixing are four: three angles $(\theta_{12}, \theta_{13}, \theta_{23})$ and the CP violating phase δ_{CP}. The PMNS matrix is also multiplied by the so called Majorana phase matrix which does not affect, however, oscillation phenomena:

$$\begin{pmatrix} e^{i\alpha} & 0 & 0 \\ 0 & e^{i\beta} & 0 \\ 0 & 0 & 1 \end{pmatrix} \tag{1.22}$$

In vacuum the probability of transition between two families can be written as

$$\begin{aligned} P(\alpha \to \beta)(t) = \delta_{\alpha\beta} - 4 \sum_{k>l=1}^{3} Re(U_{\alpha k} U^*_{\beta k} U^*_{\alpha l} U_{\beta l}) \sin^2\left(\frac{\Delta m^2_{kl} L}{4E}\right) \\ +4 \sum_{k>l=1}^{3} Im(U_{\alpha k} U^*_{\beta k} U^*_{\alpha l} U_{\beta l}) \sin\left(\frac{\Delta m^2_{kl} L}{4E}\right) \cos\left(\frac{\Delta m^2_{kl} L}{4E}\right) \end{aligned} \tag{1.23}$$

The oscillatory behaviour in general case involves three mixing angles involved as well as two mass differences Δm^2_{21} and Δm^2_{32} that set two distinct oscillation frequencies.

If we consider only two families of neutrinos e.g. ν_μ and ν_e , the unitary transformation 1.10 become

$$\begin{pmatrix} \nu_e \\ \nu_\mu \end{pmatrix} = \begin{pmatrix} \cos\theta & \sin\theta \\ -\sin\theta & \cos\theta \end{pmatrix} \begin{pmatrix} \nu_1 \\ \nu_2 \end{pmatrix} \tag{1.24}$$

where θ is the mixing angle. Considering $\Delta m^2 = m_2^2 - m_1^2$ and this matrix U we obtain the transition probability

$$P(\nu_e \to \nu_\mu) = \sin^2 2\theta \sin^2\left(\frac{\Delta m^2 L}{4E}\right) \tag{1.25}$$

This formula shows that oscillations only occur if both θ and Δm^2 are different from zero. If we express Δm^2 in (eV/c^2), L in km, E in GeV and we include the relevant values of π and c, the transition probability become

$$P(\nu_e \to \nu_\mu) = \sin^2 2\theta \sin^2\left(1.267\frac{\Delta m^2 L}{E}\right) \tag{1.26}$$

This equation means that, including only two families, if we produce a pure ν_μ beam, at distance L it will be composed by both types of neutrino and the probability of conversion, for fixed L and beam energy E, is defined by two parameters: θ and Δm^2.

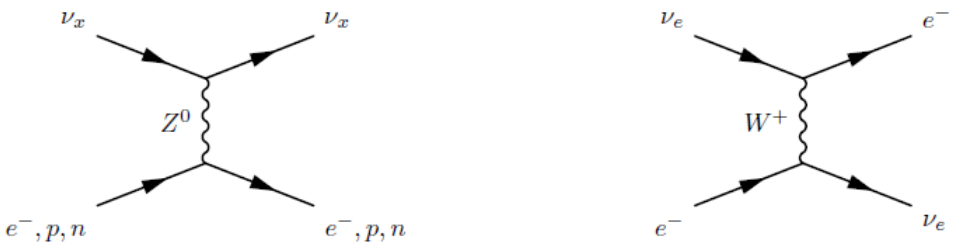

Figure 1.3: Left imagine shows Neutral Current(NC) neutrino interaction with matter. Right imagine shows Charged Current (CC) neutrino interaction with matter.

1.3.2 Neutrino oscillation in matter

We have studied the oscillation phenomenon assuming that neutrinos propagate in vacuum. We now will take into account that neutrinos interact with matter. Even if the probability of interaction of the neutrinos with matter is very low (neutrino interacts only via the weak force), this possibility changes significantly the mixing behaviour. In particular in matter ν_e can have neutral current (NC) and charged current (CC) interactions (like we can see in Figure 1.3) also with electrons, while ν_μ and ν_τ can have the same type of NC interaction but they do not interact via CC with electrons and in matter there aren't particle like μ or τ. This is called Mikheyev-Smirnov-Wolfenstein effect.

If we consider the simple two flavour case, the effective Hamiltonian in the flavour bases is described by two terms:

$$H_M = H_0 + H_{int} = \frac{\Delta m^2}{4E} \begin{pmatrix} -\cos(2\theta_V) & \sin(2\theta_V) \\ \sin(2\theta_V) & \cos(2\theta_V) \end{pmatrix} + V_{CC} \begin{pmatrix} 1 & 0 \\ 0 & 0 \end{pmatrix} \tag{1.27}$$

where V_{CC} is the representation of extra energy acquired by ν_e by CC interactions with electrons in matter and θ_V is the mixing angle. The CC interaction potential V_{CC} is defined by:

$$V_{CC} = \pm\sqrt{2} G_F n_e \tag{1.28}$$

G_F is the Fermi's constant, n_e is the electron number density and the $\pm$ is respectively for neutrinos and anti-neutrinos. The matter effects can be seen in the solar neutrino oscillation. This oscillation occurs between two flavours: the produced ν_e oscillates into another state ν_x that is a linear combination of ν_μ and ν_τ.

1.4 Neutrino sources

Various experiments have observed neutrino properties unexpected in the Standard Model. This has led to a strong development in the study of neutrino physics, which exploits, and has exploited, different types of neutrino sources to broaden the range of observable neutrino energies and to seek confirmations, or not, of the neutrino physics

models beyond the Standard Model. Four different neutrino sources are used: solar neutrinos, atmospheric neutrinos, reactor anti-neutrinos and accelerator neutrinos.

1.4.1 Solar neutrinos

During the 20th century, one model came to be the widely accepted description of the reactions in the Sun, was the Solar Standard Model (SSM). This theory considered the Sun as a natural nuclear fusion reactor, powered by two types of chain reactions (Figure 1.4). As we can see from the Figure 1.5, the possible energy spectrum for a neutrino strongly depends on the reaction that generated it. This means that not all experiments observe all solar neutrinos, but these depend on what is the threshold energy of the reaction that the experiment uses to identify neutrinos. The first experiment on

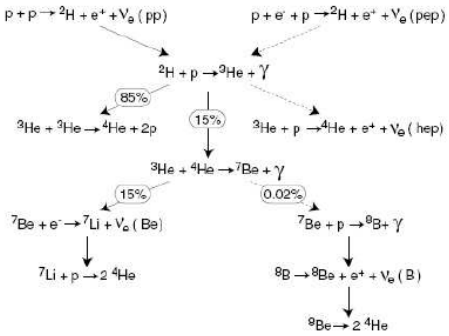

Figure 1.4: Different fusion reactions in the Sun producing neutrinos.

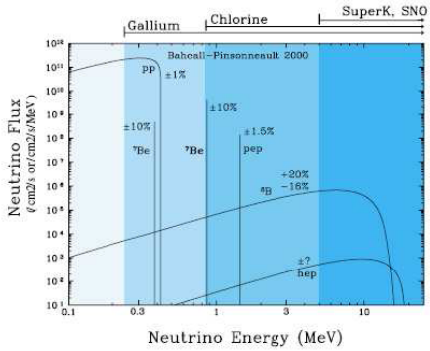

Figure 1.5: Flux of neutrinos from the Sun. According to their energy, neutrinos are accessible at the different experiment.

solar neutrino was the R. Davis's experiment in the Homestake Gold Mine, called the Homestake Experiment. The experiment used a tank of 400 m^3 of C_2Cl_4 at depth of 1.5 km, necessary to shield the cosmic rays background, to detect ν_e by inverse beta decay. The counting of the number of Ar nuclei produced by the reaction

$$Cl + \nu_e \rightarrow Ar + e^- \tag{1.29}$$

that has a threshold energy of 0.814 MeV, gives the electron neutrino flux. The typical ν_e flux reaching the Earth is approximately $10^{10}\frac{\nu_e}{s \cdot cm^2}$. The result of this counting was that the ν_e detected from the Sun are only about one third of those expected by the theoretical prediction of the SSM. There were three kinds of explanation proposed to solve this problem:

- the SSM was wrong;
- the Homestake experiment made wrong measurement;

- the SM of neutrino was wrong.

The first and second explanations are now conclusively ruled out. The SSM does accurately predict the brightness of the Sun but not the number of neutrinos, so presumably the problem was in the description of the properties of neutrinos and not in the model. To exclude a measurement problem, an accurate calibration analysis was performed, and the results were confirmed. Furthermore, independent experiment, like Super-Kamiokande, showed a deficit as well, thus demonstrating that the second explanation is also wrong. The only solution left to explain the deficit of solar neutrinos was that their description in SM was not correct. The theoretical solution follows from considering massive neutrinos, so the possibility of neutrino oscillation, that would explain the deficit observed in those experiments that could only see ν_e. The proof of this would be an experiment able to prove that the total neutrino flux was conserved.

The solution was established in 2002 by the SNO experiment. SNO is a heavy water (D_2O) Cherenkov detector, whose great innovation was the sensitivity not only to the ν_e charged current interaction but also to the neutral current interactions of neutrinos of any flavour with the Deuterium nuclei. The free neutron is then detected and with this measurement it is possible to measure the total solar neutrino flux.

Comparing the measured flux from the charged and the neutral current interactions we have

$$\begin{aligned} \phi_{CC} = \phi_e &= 1.70 \pm 0.07(stat)^{+0.09}_{-0.10}(syst) \cdot 10^6 \frac{\nu}{cm^2 s} \\ \phi_{NC} = \phi_e + \phi_\mu + \phi_\tau &= 4.90 \pm 0.24(stat)^{+0.29}_{-0.27}(syst) \cdot 10^6 \frac{\nu}{cm^2 s} \end{aligned} \tag{1.30}$$

The measurement of the fluxes demonstrated that solar neutrinos, born as ν_e, arrive on the earth as a mix of ν_e, ν_μ and ν_τ of which ν_e is only one third. This result is the final clarification of the solar neutrino puzzle. The fluxes in 1.30 are different from the total expected neutrino flux since SNO experiment was sensitive only to high energy neutrinos coming from the ^8B reaction.

1.4.2 Atmospheric neutrinos

When the flux of cosmic rays particles, primarily protons, enters the atmosphere, it interacts with its nuclei producing a huge number of secondary particles, in particular pions. These particles then decay in flight via $\pi^\pm \to \mu^\pm + \nu_\mu(\bar{\nu}_\mu)$. The produced muons then decay according to $\mu^\pm \to e^\pm + \nu_e(\bar{\nu}_e) + \bar{\nu}_\mu(\nu_{mu})$.

The typical energy spectrum of atmospheric neutrinos starts at about hundred MeV and extends up to several GeV. This source cannot be to approximated as a point-like source so the measurement of neutrino oscillation requires a different technique. Neutrinos can be generated at any point of the atmosphere so they can travel very different

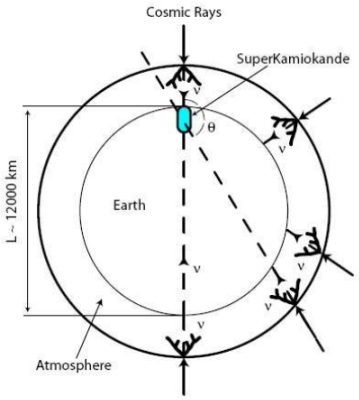

Figure 1.6: Different flight distances, between the production point and Super-Kamiokande, for neutrinos produced in cosmic ray interactions with Earth atmosphere.

distances before reaching the detector and this gives different oscillation probabilities (see Figure 1.6). To study the oscillation probability it is necessary to have detectors able to recognize the direction of the incident neutrino and the water Cherenkov technique proved to be the most effective for this purpose.

In general when neutrinos interact with matter via the charged current they generate leptons. If they interact in water and if the lepton energy is above the water Cherenkov threshold, which is few MeV for electrons and few hundreds MeV for muons, light is emitted on a cone centred on the lepton trajectory. The typical water Cherenkov detector is composed of a huge water tank equipped with an array of phototubes mounted on its wall used to record the Cherenkov light. If the lepton stops inside the detector, the amount of Cherenkov light is used to determine the energy of the lepton, and hence of its neutrino parent. Moreover muons and electrons can be separated by the shape of their Cherenkov rings, giving in this way also the flavour of the primary neutrino, but the detector cannot measure the charge of the final state leptons and therefore neutrino and anti-neutrino induced events cannot be discriminated.

The larger detector of this type is SuperKamiokande, a 50 kton water Cherenkov detector. The experiment counts ν_e and ν_μ in bins of the zenith angle $\theta(\cos\theta = 1$ for the neutrinos coming from the zenith and $\cos\theta = -1$ if they come from the nadir) and the events are subdivided in two energy categories, sub-GeV(visible energy below 1.33 GeV) and Multi-GeV (visible energy above 1.33GeV) [20] [17]. The zenith angle distribution of the μ-like events shows a strong deviation from no oscillation hypothesis, in reverse the zenith angle distribution of e-like events is consistent with the expectation. The only possible explanation is that atmospheric ν_μ transform into a linear superposition of neutrinos, with small ν_e content, since there is no excess in the ν_e flux coming from the opposite side of the Earth.

1.4.3 Reactor anti-neutrinos

Nuclear reactors are copious sources of electron anti-neutrinos produced in the β-decay of neutron rich nuclei. The power of the reactor is mainly due to the fission of four isotopes ^{235}U, $^{138}U(\sim 8\%)$, $^{239}Pu(\sim 30\%)$ and $^{241}Pu(\sim 6\%)$. Since, on average, each fission produces about 200 MeV, releasing about six $\overline{\nu}_e$'s, the electron anti-neutrino yield is about $2 \times 10^{20} s^{-1}$ for each GW of thermal power. Typical light-water nuclear power plants have several reactor cores, each with a thermal power of the order of 3 GW. The total rate of anti-neutrino flux is isotropic and it decreases quadratically with distance. This is a problem for neutrino oscillation experiments, which require an appropriately long source-detector distance in order to reveal the oscillations. The anti-neutrino energy spectrum is in the same range (few MeV) of the Solar neutrinos so in reactors experiment only the $\overline{\nu}_e$ disappearance can be investigated, since the energy is not sufficient to produce muons or taus from CC reaction.

In 2002 the first evidence of oscillation of reactor neutrinos was found by the KamLAND experiment.KamLAND is a 1 kton ultra-pure liquid scintillator detector located at the old Kamiokande's site in Japan, and detects $\overline{\nu}_e$ coming from 16 reactors located at an average distance of 160 km (Figure 1.7).

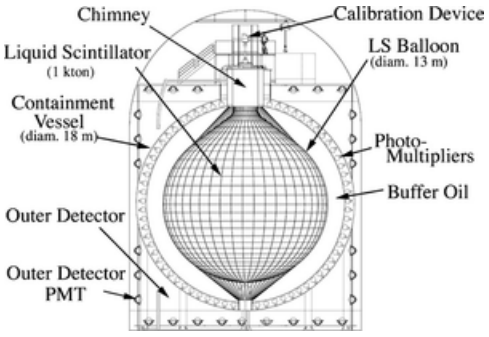

Figure 1.7: Schematic view of KamLAND detector.

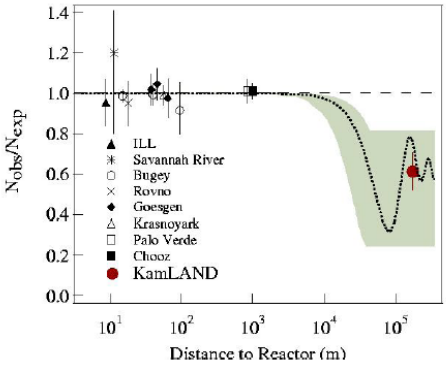

Figure 1.8: Ratio of measured neutrinos over expected neutrinos versus the distance of different reactor anti-neutrino experiments.

When an electron anti-neutrino is captured by a free proton, an inverse β-decay reaction can occur. In this case the positron losses its energy and annihilates, yielding two γ-rays (each 511 keV). The neutron thermalizes in $211.2 \pm 2.6 \mu s$ and is then captured by a proton in the reaction $n + p \rightarrow d + \gamma$ $(2.22\ MeV)$ [14]. The delayed coincidence of γ-rays generated from those prompt positron and those produced from the capture of neutron, is the signature that is used by KamLAND for their measurement. This is the same method that Reines and Cowan used in their experiment. This experiment has a

sensitive Δm^2 range down $\sim 10^{-5} eV^2$. The first KamLAND results (1.8) showed that the ratio of observed to expected (assuming no $\overline{\nu}_e$ oscillations) number of events was:

$$\frac{N_{obs} - N_{BG}}{N_{NoOsc}} = 0.611 \pm 0.085(stat.) \pm 0.041(syst.) \tag{1.31}$$

Another interesting result coming from a reactor experiment was published by CHOOZ collaboration in 1999. At that time, CHOOZ produced the most significant limit on the neutrino mixing angle θ_{13} that was the last mixing angle parameter to measure in the PMNS matrix. This experiment was located in France and used anti-neutrinos coming from two reactors, which are able to provide a pure source ($> 99.9\%$) of $\bar{\nu}_e$. The upper limits measured was $\theta_{13} < 10^\circ$ for $\Delta m^2_{13} = 3 \times 10^{-3} eV$. More recently, in 2012, three reactor experiments were able to measure the mixing angle θ_{13}: Daya Bayin China, RENO in South Korea and the Double-CHOOZ experiment in France. They found [10], [13], [4]:

$$\begin{aligned} \sin^2 2\theta_{13|DayaBay} &= 0.084 \pm 0.005(stat. \ + \ syst.) \\ \sin^2 2\theta_{13|RENO} &= 0.082 \pm 0.009(stat.) \pm 0.006(syst.) \\ \sin^2 2\theta_{13|Double-CHOOZ} &= 0.088 \pm 0.033(stat. \ + \ syst.) \end{aligned} \tag{1.32}$$

Reactor experiments give the cleanest θ_{13} measurement because they are not sensitive to any other oscillation parameter.

$$P(\bar{\nu}_e \to \bar{\nu}_e) \approx 1 - \sin^2 2\theta_{13} \sin^2(1.27 \Delta m^2_{13} L/E) \tag{1.33}$$

1.4.4 Accelerator neutrinos

The accelerator experiment can be classified according to the method of production of neutrino beam: Pion Decay in Flight (DIF), muon Decay At Rest (DAR) and beam dump. The characteristics of each one of those neutrino beam are:

- **Pion DIF**: these are the experiments with a neutrino beam composed mainly of muon neutrinos produced by decay of pions and kaons initially produced by a proton beam hitting a target. Some experiments that used the pion decay in flight technique to produce the neutrino beam were CHORUS, NOMAD, OPERA, MINOS and now T2K and NOνA.

- **Muon DAR**: these experiment use the π^+ and μ^+, most of which decay at rest, decay reaction as source of anti-neutrino beam. Typically the energy of $\overline{\nu}_\mu$ produced in muon DAR is of the order of several tens of MeV and can be used to measure the oscillation $\overline{\nu}_\mu \to \overline{\nu}_e$. Some experiments used this technique, like LSND and KARMEN.

- **Beam Dump**: Also called prompt neutrino experiments. In this case a very high energy proton beam, of a few hundred GeV, is completely stopped in a thick

target, called the beam dump, where the proton nucleon interactions generate heavy hadrons. The charmed heavy hadrons decay promptly with practically equal branching ratios into electrons and muons, emitting equal fluxes of electron and muon neutrinos with energies of several tens of GeV on average (up to above 100 GeV). Some experiments that used the beam dump technique to produce the neutrino beam were CBEBC and CHARM.

In addiction, the experiments with neutrino beams generated by pion decay in flight are further classified in three categories:

- **Wide Band (WB) beam**: have a high-intensity neutrino beam with a wide energy spectrum which can span one or two orders of magnitude. This type of beam is convenient for investigating new oscillation signals in a wide range of values of Δm^2.
- **Narrow Band (NB) beam**: these experiments have a narrow energy spectrum, which is obtained with the selection of the neutrino parents (pions and kaons) momenta. The resulting intensity of the neutrino flux of a NB beam is reduced comparing with a WB beam obtained from the same proton beam. NB beams are convenient for precise measurements of Δm^2.
- **Off-Axis (OA) beam**: use a high-intensity WB beam with the detector shifted by a small angle with respect to the axis of the beam, where the neutrino energy is almost monochromatic.

According to the average distance between source and detector experiments are classified as:

- Short BaseLine (SBL): $L \sim 10m - 1km$
- Long BaseLine (LBL): $L \sim 10^2 - 10^4 km$

The strong dependence of neutrino oscillation on $\frac{L}{E}$ implied that LBL experiments were more productive than SBL experiments in the measurement of neutrino oscillation parameters. Only the Liquid Scintillation Neutrino Detector (LSND) experiment found a signal of $\bar{\nu}_\mu \to \bar{\nu}_e$ and weaker signal in $\nu_\mu \to \nu_e$. This experiment used a 798 MeV proton beam at the Los Alamos Neutron Science Center(LANSCE) to produce charged pions. The π^- were mostly absorbed and only a small fraction decay into μ^-, which in turn were largely captured. The resulting neutrino source was dominantly due to $\pi^+ \to \mu^+ + \nu_\mu$ and $\mu^+ \to e^+ + \nu_e + \bar{\nu}_\mu$ decays, most of which decay at rest [7]. The experiment used the reaction $\bar{\nu}_e + p \to e^+ + n$, which had a large and well known cross section, to search evidence of $\bar{\nu}_\mu \to \bar{\nu}_e$ oscillation. The LSND experiment took data over six years (1993-1998) and it observed an excess of events consistent with neutrino oscillations hypothesis.

MiniBooNE experiment detect neutrinos and anti-neutrinos created in Booster Neutrino Beamline at Fermilab using a 445 ton fiducial volume mineral oil detector surrounded by 1280 photomultiplier tubes. MiniBooNE has recently reported a 4.5σ excess

of ν_e-like events in a neutrino mode search for $\nu_\mu \to \nu_e$ oscillations via charged current quasi-elastic scattering. This measurement are also consistent with the 3.8σ excess in $\bar{\nu}_e$ appearance reported by the LSND [19].

The typical method used by the LBL experiment is to measure the neutrino beam at two points: one near the neutrino production point, the other after the oscillation in a far detector.
The K2K (KEK to Kamioka) was the first long beseline accelerator neutrino experiment and it had as goal the confirmation of the atmospheric ν_μ disappearance observed at Super-Kamiokande(SK). They used an accelerator-produced beam of nearly pure ν_μ to probe the same Δm^2 region as that explored with atmospheric neutrinos. Neutrinos were measured first by a suite of detectors (a 1 kT water tank Cherenkov detector and a fine grained system) at the approximately distance of approximately 300 m from the neutrino production point, and then by Super-Kamiokande detector 250 km away. The K2K experiment took data between 1999 and 2004 and it observed 112 fully contained (all light was generated inside the water tank fiducial volume) events in the 22.5 kton fiducial volume of SK, compared with an expectation of $158.1^{+9.2}_{-8.6}$ events without oscillation [9].

Another exemple of LBL experiment was MINOS (Main Injector Neutrino Oscillations). The beam was produced by the NuMI facility (Neutrinos at the Main Injector) using protons accelerated up to 120 GeV by the Fermilab Main Injector. The channels used by MINOS to find oscillation parameters were ν_μ disappearance and ν_e appearance. The combined analysis of the ν_μ disappearance and ν_e appearance data along with atmospheric neutrino data reported $|\Delta m^2_{32}| = (2.28 - 2.46) \times 10^{-3} eV^2 (68\% C.L.)$ and $\sin^2\theta_{23} = 0.35 - 0.65 (90\% C.L.)$ in the normal hierarchy, and $|\Delta m^2_{32}| = (2.32 - 2.53) \times 10^{-3} eV^2 (68\% C.L.)$ and $\sin^2\theta_{23} = 0.34 - 0.67 (90\% C.L.)$ in the inverted hierarchy [5]. The successor of MINOS is NOνA (Numi Off-axis ν_e Appearance) that consists of two detectors, one at the Fermilab (near detector), and one in northern Minnesota (the far detector). Neutrinos pass through 810 km of Earth. Last NOνA announced results are: $\Delta m^2_{32} = 2.51^{+0.12}_{-0.08} \times 10^{-3} eV^2$,$\sin^2 2\theta_{23} = 0.58 \pm 0.03$ and $\delta_{CP} = 0.17\pi$[18].

OPERA (Oscillation Project with Emulsion-tRacking Apparatus) was an experiment located at Gran Sasso, Italy. This experiment has been designed to search for $\nu_\mu \to \nu_\tau$ oscillation in appearance mode through the detection of the τ lepton produced in the ν_τ charged current interactions. The detector at the LNGS underground laboratory has been exposed from 2008 to 2012 to the CERN neutrinos to the Gran Sasso (CNGS) ν_μ beam. The experiment reported the discovery of ν_τ appearance in a muon neutrino beam with a 6.1σ significance, by reporting 10 ν_τ candidates, thus confirming the atmospheric ν_μ oscillation into ν_τ.[6].

Chapter 2

T2K experiment

The T2K (Tokai-to-Kamioka) experiment is a long baseline neutrino oscillation experiment designed with the purpose to measure the last unknown mixing angle (θ_{13}) in the lepton sector by observing ν_e appearance in a ν_μ beam. In addition, T2K aims at determining oscillation parameters Δm^2_{23} and $\sin^2 2\theta_{23}$ with precision of $\delta(\Delta m^2_{23}) \sim 10^{-4}$ and $\delta(\sin^2 2\theta_{23}) \sim 0.01$ via ν_μ disappearance studies. Other goals of the experiment are cross section measurement, sterile neutrino searches and the measure of δ_{CP}. The experiment uses an intense proton beam generated by the J-PARC accelerator in Tokai, Japan, and is composed of a neutrino beam-line, a near detector complex (INGRID and ND280), and a far detector (Super-Kamiokande) located 295 km away from J-PARC (Figure 2.1).

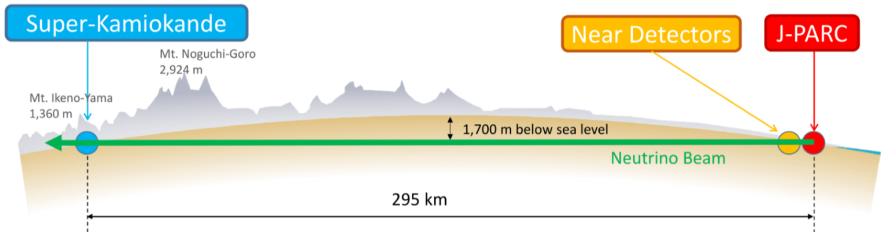

Figure 2.1: A schematic of a neutrino's journey in T2K.

2.0.1 ν_e appearance and ν_μ disappearance results

Already in 2011, with only 4% of the total approved data, T2K was the first experiment in the world to give an indication of $\theta_{13} \neq 0$ with a C.L. of 2.5σ. Reactor experiment confirmed the result with higher statistical significance. T2K began collecting data in anti-neutrino mode in May 2014 to search for anti-neutrino oscillation. The last results on δ_{CP}, $\sin^2 2\theta_{23}$ and Δm^2 (Δm^2_{32} for normal or Δm^2_{32} for inverted ordering) are obtained by analysing both muon (anti-) neutrino disappearance and electron (anti-) neutrino appearance data collected from Jan 2010 to May 2017. The data sets include a beam

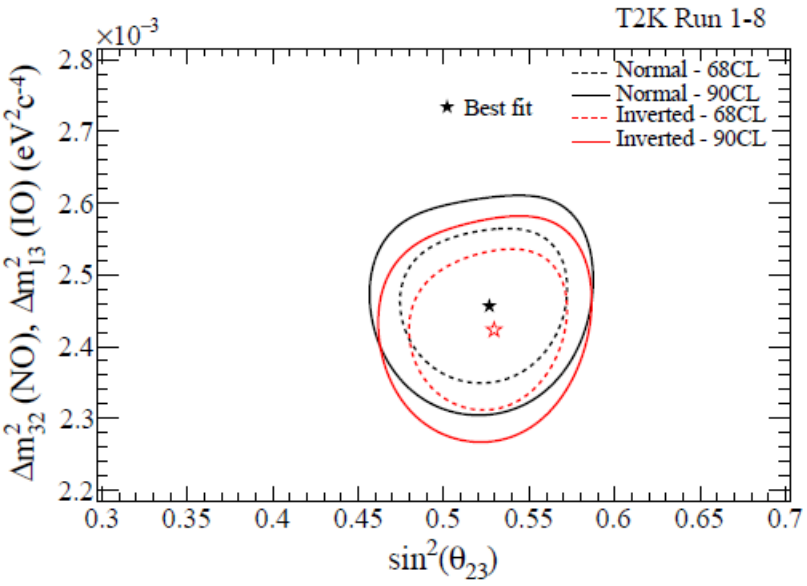

Figure 2.2: The 68%(90%) constant confident regions in $|\Delta m^2| - \sin^2 2\theta_{23}$ plane for normal(black) and inverted(red) ordering using reactor measurement prior on $\sin^2 2\theta_{13}$.

exposure of 14.7×10^{20} protons on target in neutrino mode and 7.6×10^{20} POT in anti-neutrino mode for the far-detector analysis, and an exposure of 5.8×10^{20} POT in neutrino mode and 3.9×10^{20} POT in anti-neutrino mode for the near-detector (ND280) analysis.

To constrain oscillation parameters T2K used a joint maximum-likelihood fit. Priors for flux and interaction cross-section parameters are found using results from a fit to the near detector data. The results with 1σ errors for $\sin^2 2\theta_{23}$ and Δm^2_{32} (Figure 2.2) are:

$$\begin{aligned} \sin^2 2\theta_{23} &= 0.526^{+0.032}_{-0.036} N.O. \\ \sin^2 2\theta_{23} &= 0.530^{+0.030}_{-0.034} I.O. \\ \Delta m^2_{32} &= 2.463^{+0.071}_{-0.070} \times 10^{-3} \frac{eV^2}{c^4} N.O. \\ \Delta m^2_{32} &= 2.432^{+0.070}_{-0.070} \times 10^{-3} \frac{eV^2}{c^4} I.O. \end{aligned} \tag{2.1}$$

Confidence regions in the $\sin^2 2\theta_{13} - \delta_{CP}$ (Figure 2.3) plane were calculated, without using the reactor measurement prior on $\sin^2 2\theta_{13}$, for both the normal and inverted order.

The reactor measurement prior ($\sin^2 2\theta_{13}$) is used for the δ_{CP} fit. The best fit value of it is -1.87 (-1.43) for the normal (inverted) ordering, which is close to maximum CP violation. The δ_{CP} confidence intervals at 2σ (95.45%) are (-2.99,-0.59) for normal ordering and (-1.81,-1.01) for inverted ordering. Both intervals exclude the CP-conserving values of 0 or π [2].

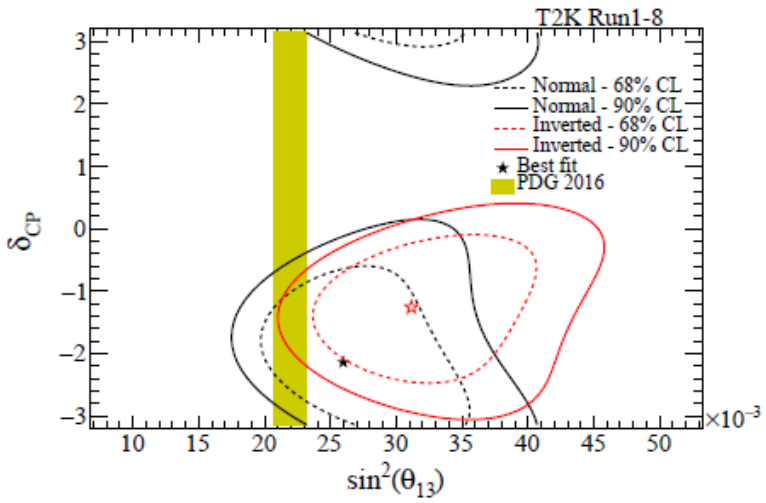

Figure 2.3: The 68%(90%) confidence regions in the $\sin^2 2\theta_{13} - \delta_{CP}$ plane using a flat prior on $\sin^2 2\theta_{13}$, assuming normal (black) and inverted (red) mass ordering. The 68% confidence region from reactor experiments on $\sin^2 2\theta_{13}$ is shown by yellow vertical band.

2.1 The off-axis technique

T2K adopts the off-axis method to generate a narrow-band neutrino beam using the proton synchrotron at J-PARC. This technique was first proposed by D. Beavis et al. [11] and allows the production of an almost monochromatic neutrino beam, that is mainly composed of ν_μ, or $\bar{\nu}_\mu$, neutrinos coming from pion decays. Then the beam heads to the near and far detector that sit along a line at an angle of 2.5° respect to axis of the beam. Another advantage of this method is that it cuts the high energy tail present in the neutrino beam removing backgrounds like NC and charged-current non quasi-elastic(CCnQE) interactions.

To better understand the off-axis method, let us consider the ideal case where it is possible to obtain a pure π^+ beam, produced by interaction of a proton beam with a graphite target. The pions will decay with a $BR \sim 99.9\%$ according to

$$\pi^+ \rightarrow \mu^+ + \nu_\mu \tag{2.2}$$

In the pion rest frame the neutrino has a maximal energy given by:

$$E^*_{\nu,Max} = \frac{m_\pi^2 - m_\mu^2}{2m_\pi} = 29.8 MeV \tag{2.3}$$

where $*$ indicates quantities in pion rest frame. The neutrino four-momentum, for $|\vec{P}_\nu| \gg m_\nu$, will be in the laboratory frame:

$$P_\nu = (E_\nu, E_\nu \sin\theta, 0, E_\nu \cos\theta) \tag{2.4}$$

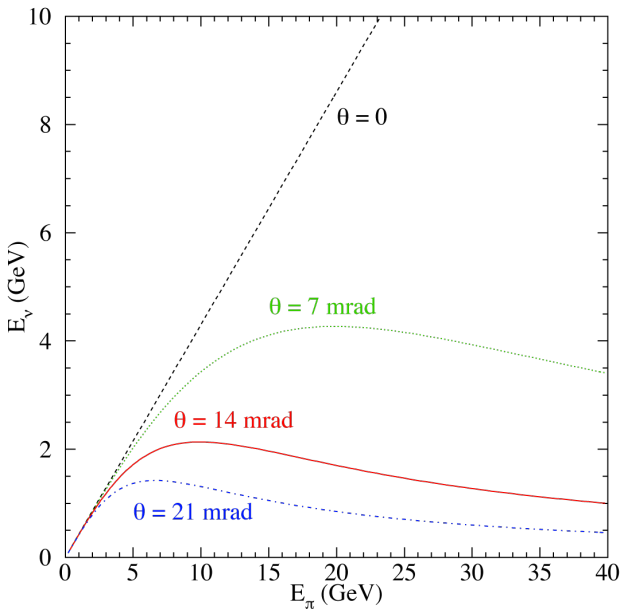

Figure 2.4: Expected neutrino energy as a function of the parent pion energy for different values of the off-axis angle.

where θ is the angle between neutrino and pion direction. If now we use the Lorentz boost $\gamma_\pi = \frac{E_\pi}{m_\pi}$, in the laboratory frame, 2.4 becomes:

$$P_\nu = (\gamma_\pi E^*_\nu(1 + \beta_\pi \cos\theta^*), E^*_\nu \sin\theta^*, 0, \gamma_\pi E^*_\nu(\beta_\pi + \cos\theta^*)) \tag{2.5}$$

The decay is isotropic in the pion rest frame because the pion has spin zero, so we can derive a relation for the angle θ from 2.4, 2.5, and considering $\beta_\pi \sim 1$:

$$\tan\theta \sim \frac{E^*_\nu \sin\theta^*}{\gamma_\pi E^*_\nu(1 + \cos\theta^*)} \sim \frac{E^*_\nu \sin\theta^*}{E_\nu} \tag{2.6}$$

Since $\sin\theta^* < 1$, in the laboratory frame there is a maximum angle at which the neutrino of energy $E_{\nu(\bar{\nu})}$ can be emitted. Using 2.3 the maximum angle is:

$$\theta_{max} \sim \frac{E^*_\nu}{E_\nu} \sim \frac{30MeV}{E_\nu} \tag{2.7}$$

so we can write

$$E_\nu \sim \frac{E^*_\nu \sin\theta^*}{\tan\theta} \leq \frac{E^*_\nu}{\tan\theta} \tag{2.8}$$

So if $\theta \neq 0$ there is a maximum energy at which neutrinos can be emitted, while if $\theta = 0$ the energy of neutrino is proportional to the energy of the parent pion (Figure 2.4). For $\theta = 2.5°$, this correspond to $E_\nu \leq 682MeV$ in the laboratory frame.

The choice of this specific angle has three advantages for T2K studies. The first is that at

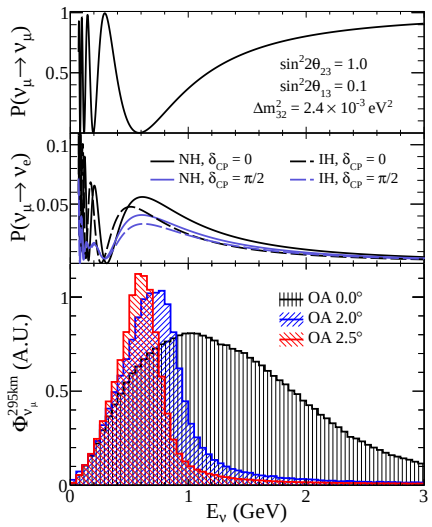

Figure 2.5: Muon neutrino disappearance and electron neutrino appearance probability at 295 km compared to the neutrino fluxes for different off-axis angles. The neutrino beam at SK has a peak energy at about 0.6 GeV maximizing the effect of the neutrino oscillations at 295 km.

the energy of $\sim$ 600 MeV, at the distance of 295 km, with $\sin^2 2\theta_{23} = 1.0$, $\sin^2 2\theta_{13} = 0.1$ and $\Delta m^2_{23} = 2.4 \times 10^{-3} eV^2$, the probability of the ν_μ disappearance and ν_e appearance are near an stationary point of function (as shown in Figure 2.5).The second advantage is that at the angle of $\theta = 2.5°$ the flux of ν_μ generated has a very narrow peak exactly around the energy point helpful for oscillation studies. The third advantage is to reduce one of two main backgrounds to the ν_e appearance signal, i.e. the contamination of ν_e that come from decays of muons and kaons according to the following relations:

$$\mu^\pm \rightarrow e^\pm + \bar{\nu}_\mu(\nu_\mu) + \nu_e(\bar{\nu}_e) \tag{2.9}$$

and

$$K^+ \rightarrow \pi^0 + e^+ + \nu_e \tag{2.10}$$

In fact, these are both 3 body decays, while the off-axis strategy enhances neutrinos coming from two body decays.

2.2 J-PARC accelerator

J-PARC (Japan Proton Accelerator Research Complex) is a high intensity proton accelerator facility located in Tokai village in the northern region of Ibaraki prefecture, in Japan. The accelerator complex is composed by three parts: a linear accelerator (LINAC), a rapid-cycling synchrotron (RCS) and the main ring (MR) synchrotron.
An H^- beam is accelerated up to 400 MeV by the LINAC, and is converted to an H^+

beam by charge-stripping foils at the RCS injection, after this the beam is accelerated up to 3 GeV. Only the 5% of bunches are supplied to the MR, the rest of bunches are supplied to the muon and neutron beam-line in the Material and Life Science Facility. In the MR, the proton beam is accelerated up to 30 GeV. There are two extraction points in the MR: slow extraction point for the hadron beam-line and fast extraction point for the neutrino beam-line.
In the fast extraction mode, eight circulating proton bunches are extracted within a single turn by a set of five kicker magnets then the beam goes to the neutrino beam-line. The time structure of the extracted proton beam is really important because it is used as trigger for acquisition and, in this way, it is the key to discriminate various backgrounds, including cosmic rays, in the various neutrino detectors.

2.2.1 T2K neutrino beamline

The neutrino beam-line is divided in two sections: the primary and secondary beam-line. The primary beam-line consists of three sections: a preparation section to tune the beam extracted from the MR, an arc section to bend the beam towards Kamioka, and a final focusing section to focus the beam onto the target. Normal-conducting magnets are used for the preparation section and final focusing section. An Overview of the neutrino beam-line is shown in Figure 2.6.

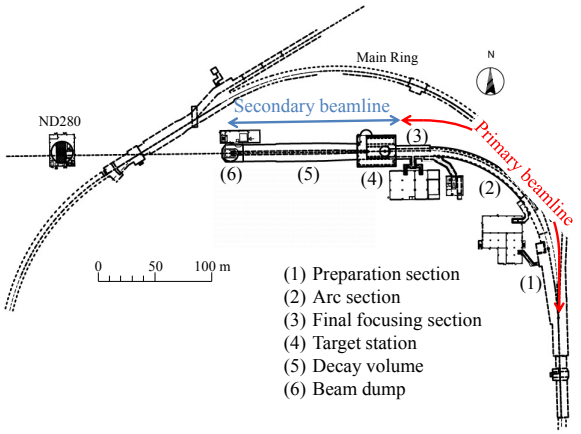

Figure 2.6: Overview of the T2K beamline.

The intensity, position, profile and loss of the proton beam are precisely monitored by different type of sensors because a well-tuned proton beam is essential for a stable neutrino beam production.
The secondary beam-line is composed by three "big" parts(Figure 2.7): target station, decay volume and beam dump. The target station is connected to the primary beam-line by a beam window that is composed by two helium-cooled 0.3 mm thick titanium-alloy. After the beam window there is a baffle which is a collimator 1.7 m long, 0.3 m wide and 0.4 m high graphite block, with a hole of 30 mm for the proton beam. In this way

the beam is completely focused on the target, but upstream there is a *Optical transition Radiation Monitor* that it is used to measure the profile of the proton beam.

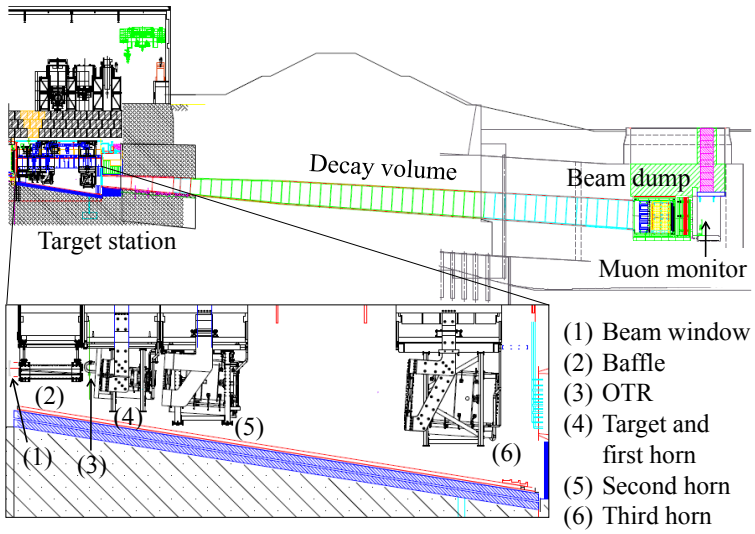

Figure 2.7: Side view of the secondary beamline.

The target core is a 91.4 cm long, 2.4 cm diameter graphite rod and it is sealed into a titanium case which is 0.3 mm thick. The target assembly is located into the bore of the first inner conductor of the first magnet (horn). The graphite was chosen because a significantly denser and higher Z material than graphite would be melted by the pulsed beam heat load. The interaction of the protons on graphite generate pions and kaons that will decay into neutrinos.
The T2K experiment uses 3 magnetic horns to collect and focus the pions exiting the target. Each magnetic horn consists of two coaxial conductors that create a toroidal magnetic field. The field varies as $1/r$, where r is the distance from the horn axis, and when the horns are run with operation current of 320 kA, the maximum field intensity is 2.1 T. It is possible to select the charge of the pions, choosing the sign of the current in the first horn, so we can build a neutrino beam or an anti-neutrino beam. The focused hadrons, then, enter in a decay volume where they can decay according to

$$\pi^{\pm} \rightarrow \mu^{\pm} + \nu_{\mu}(\bar{\nu}_{\mu}) \tag{2.11}$$

The decay volume is a $\sim$ 94 m long steel tunnel with an increasing section; 1.4 m wide and 1.7 m high at the upstream end, 3.0 m wide and 5.0 m high at the downstream end. All the volume is surrounded by 6 m thick reinforced concrete shielding. At the end of decay volume there is a beam dump composed of 75 tons of graphite and fifteen iron plates. Only muons above $\sim 5GeV/c$ can go through the beam dump to reach

the downstream muon pit. After the beam dump there is a control muon system called the Muon Monitor(MUMON), designed to measure the neutrino beam direction with a precision better then 0.25 mrad. The MUMOM consists of two types of detectors arrays: ionization chambers and silicon PIN photodiede.

2.3 Near detector complex

At the distance of 280 m from target there is the first experimental site of T2K experiment, so called *Near Detector complex*. It consists of two parts:

- the on-axis detector: INGRID.
- the off-axis detector: ND280

2.3.1 INGRID: on-axis detector

The on-axis detector INGRID is an array of iron/scintillator detectors, centered on the neutrino beam axis. The goal of INGRID is to provide daily measurements of intensity and position of neutrino beam. The INGRID detector consists of 14 identical modules arranged as a cross of two identical groups of the 7 modules along the horizontal and vertical axis, and two additional separate modules located in the off-axis direction, as shown in Figure 2.8. The purpose of the two off-axis modules is to check the axial sym-

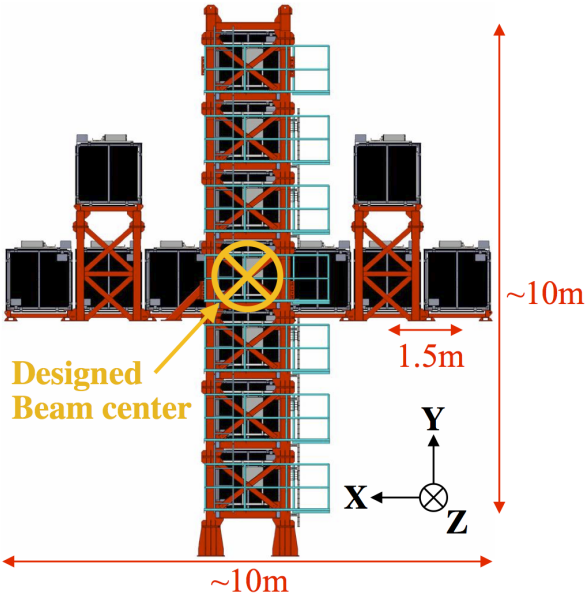

Figure 2.8: Structure of on-axis detector INGRID.

metry of the neutrino beam.
Each INGRID modules(Figure 2.9) consists of a sandwich structure of nine iron plates and 11 tracking scintillator planes. The dimensions of a iron plane is $124cm \times 124cm \times 6.6cm$

and the total iron mass used as a neutrino target is 7.1 ton. One scintillator plane is composed of 24 scintillator bars in horizontal direction glued to 24 perpendicular scintillator bars in the vertical direction. Each module is surrounded by veto scintillator planes, to reject interactions that are coming from outside. The dimensions of a scintillator bar are

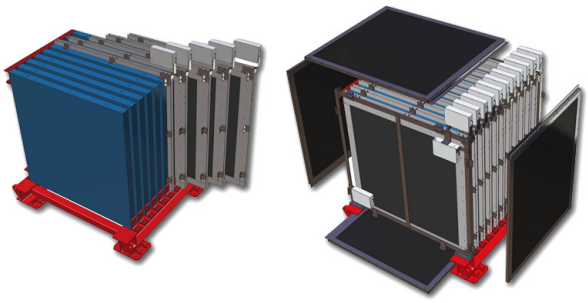

Figure 2.9: An INGRID module. The left image shows the tracking planes(blue) and iron planes (grey). The right image shows veto planes(black).

$1.0cm \times 5.0cm \times 120.3cm$. An extra module(*Proton Module*), different from the other, has been added in order to detect the proton produced with the muon in neutrino interactions with good efficiency. In this module, that is placed in the center of INGRID, there are only scintillator planes without iron planes. The purpose of this model is to identify the quasi-elastic channel for comparison with Monte Carlo simulations of beamline and neutrino interactions.

2.3.2 ND280: off-axis detector

The aims of the off-axis detector ND280 are to measure neutrino flux, neutrino energy spectrum and electron neutrino contamination in the direction of the far detector, along with measuring charged current cross-sections of ν_μ and ν_e. To reach these goals the ND280 detector must have the capability to reconstruct different type of neutrinos interaction. The first type of interaction that ND280 identify is the charged current quasi-elastic(CCQE) interaction:

$$\nu_\mu + n \rightarrow \mu^- + p \tag{2.12}$$

$$\bar{\nu}_\mu + p \rightarrow \mu^+ + n \tag{2.13}$$

respectively for ν_μ and $\bar{\nu}_\mu$ interaction. The muon momentum needs to be known with a moderate resolution because the neutrino energy reconstruction is affected by the smearing due to the Fermi motion in the nucleon target, that is of 10% for neutrinos with energies typical of the T2K beam. The other types of interaction are useful to estimate the background of different measurement. One of the major component of the

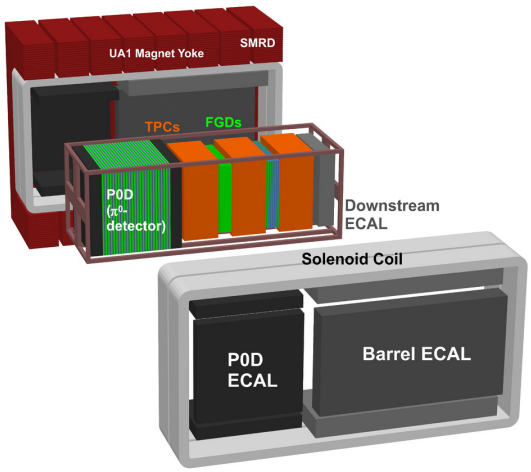

Figure 2.10: An exploded view of the ND280 off-axis detector.

background is the CCQE interaction of ν_e and $\bar{\nu}_e$. The main difficulty of the reconstruction will be to identify electrons in a sample dominated by muons with the same charge. The ν_e contamination is mainly due to kaon decays, in particular to K_{e3} decays ($K^+ \to \pi^0 + e^+ + \nu_e$).
As show in Figure 2.10, ND280 is a composed detector and it consists of:

- the PØD and TPC/FGD sandwich (tracker), both of which are placed inside of a metal frame container, called the "basket".
- An electromagnetic calorimeter (ECAL) that surrounds the basket.
- The UA1 magnet instrumented with scintillator as a muon range detector(SMRD)

2.3.3 Pi-zero detector(PØD)

The primary objective of the PØD is to measure the neutrino neutral current process:

$$\nu_\mu + N \to \nu_\mu + \pi^0 + X \tag{2.14}$$

on water (H_2O) target. i.e. cross sections for neutrino interactions that generate pi-zero's, especially the cross section for neutral current pi-zero production, which is one of the dominant sources of background to the electron neutrino appearance signal in T2K. The PØD is composed of layers of plastic scintillator alternating with water bags and brass sheets or lead sheets and is one of the first detectors to use Multi-Pixel Photon Counters (MPPCs) on a large scale. As shown in Figure 2.11, the PØD is composed by the central station ("upstream water target" and "central water target"), where there are water bags alternated with scintillator planes and brass sheets, and by the front

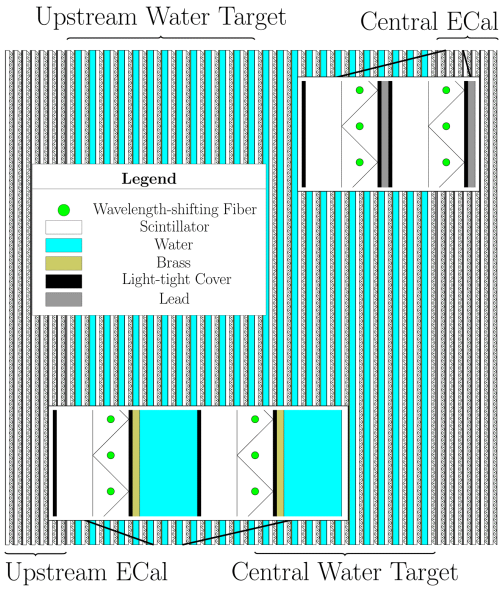

Figure 2.11: A schematic view of the pi-zero detector. The beam is coming from the left and going to right.

and rear sections ("upstream ECAL" and "central ECAL"). In these sections we find scintillator planes interchanged with lead planes, this structure is used as electromagnetic calorimeter. This layout improves the containment of electromagnetic showers and provides a veto region upstream and downstream of the water target region to provide effective rejection of particles produced outside the PØD.

There are a total of 40 scintillator modules in PØD and each of those has two perpendicular arrays of triangular scintillator bars. Each bar has a single hole filled with a WLS fiber (Kuraray double-clad Y11 of 1 mm diameter). The scintillators modules were formed into four "super-group" called super-modules. The two ECAL-PØD supermodules are a sandwich of seven modules alternating with seven stainless steel clad lead sheets (4 mm). The upstream (central) water target super-module is a sandwich of 13 modules alternating with 13(12) water bag layers (each 28 mm thick), and 13(12) brass sheets (each 1.5 mm thick). The water target layers each have two bags, for a total of 50 in the PØD detector, each with dimensions of 1006 mm$\times$ 2062 mm $\times$ 28 mm. The dimensions of the active target of the entire PØD are 2103 mm $\times$ 2239 mm $\times$ 2400 mm (width $\times$ height $\times$ length) and the mass of the detector with and without water is 16.1 tons and 13.3 tons respectively.
Determining the amount of water in the fiducial volume is critical to the PØD physics goals. The required precision is achieved by first measuring the mass vs. depth in an external buffer tank, filling the water targets to predetermined levels, and then observing the water volume removed from the tank. The water target fiducial region is designed to contain $1944 \pm 53kg$ of water, and the measured mass is $1902 \pm 16kg$.

The detector was calibrated with minimum ionizing tracks from cosmic ray muons. An average of 19 photoelectrons was obtained for the scintillator bars and 38 photoelectrons per x/y layer. The average attenuation of the pulse height in the scintillator bars from the end opposite to the PM is approximately 30%. The internal alignment of scintillator bars was checked using through-going muons with the magnet field off, and was determined to be approximately 3 mm.

2.3.4 Time Projection Chamber (TPC)

The TPCs fulfill three key functions in the near detector:

- determine the number of charged particles crossing them;
- measure the momentum of the charged particle since they operate in a magnetic field;
- identify each particle using the amount of its ionization loss energy combined with the measured momentum.

There are three TPCs (Figure 2.12) installed inside ND280, each one consists of an inner box that holds an argon-based drift gas, contained within an outer box that holds CO_2 as an insulating gas. The inner (outer) walls are made of composite panels with copper-clad G10 (aluminium) skins. The inner box panels were precisely machined to form an 11.5 mm pitch copper strip pattern which, in conjunction with a central cathode plane, produces an uniform electric drift field in the active drift volume of the TPC, roughly aligned with the field provided by the near detector magnet. When a charged particle passes through a TPC, it ionizes the gas and the electrons released with this process drift away from the cathode towards the readout planes (anode). There the electrons are multiplied and sampled with bulk micromegas (micro-mesh gas detector) detectors with 7.0 mm $\times$ 9.8 mm (vertical $\times$ horizontal) anode pad segmentation. Each readout plane is composed by twelve 342 mm $\times$ 359 mm micromegas modules, for a total of 72 modules and nearly 9 m^2 of active surface for the three TPCs. The modules are arranged in two vertical columns that are offset so that the small inactive regions between modules are not aligned. The combined information of the pattern of signals in the pad planes and the arrival time gives a complete 3D reconstructed image of the charged particle tracks. The gas system was designed to maintain a stable mixture in the inner volume, a constant positive pressure respect to the outer volume and a constant pressure between the outer volume and the atmosphere. The inner gas mixture, $Ar : CF_4 : iC_4H_{10}$ (95:3:2), was chosen for its low diffusion and good performance with micromegas detectors [3].
Particle identification is done with a truncated mean of the measurements of energy loss of the charged particle in the gas. The inner charge density of the track is estimated for each cluster by taking into account the length of the track segment corresponding to a pad column. The lowest 70% of the values are used to compute the truncated mean, an optimized approach found through Monte Carlo simulation and test beam studies. The uncertainty on the deposited energy obtained using this method is about 7.8% for

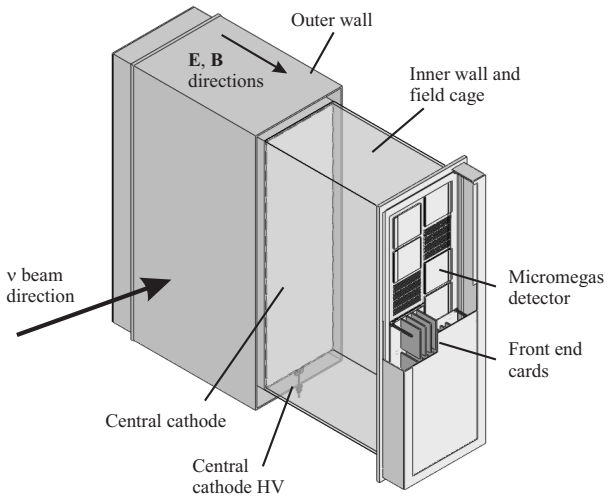

Figure 2.12: Simplified cut-away drawing showing the main aspects of the TPC design. The dimensions of whole TPC are approximately $2.3m \times 2.4m \times 1.9m$.

minimum ionizing particles, better than the design requirement of 10%.
The spatial resolution is estimated by comparing the traverse coordinate resulting from the global track fit to the one obtained with information from a single column of pad. The resolution is found typically 0.7 mm per column, in line with expectations, and degrades for increasing track angle with respect to the horizontal axis due to the ionization fluctuations along the track. The observed spatial resolution is sufficient to achieve the momentum resolution goals for the detectors.

2.3.5 Fine Grained Detector (FGD)

There are two FGDs in the off-axis detector ND280 that interleave the three TPCs, whose purpose is to provide target mass for neutrino interactions as well as tracking of charged particles coming from the interaction vertex. The two FGDs have two different designs: the first (FGD1) is composed only of scintillators layers, the second (FGD2) has alternating water and scintillator planes. This configuration gives the possibility to compare neutrino cross section on carbon and water complementary to the PØD cross section.
The FGDs are constructed from $9.61mm \times 9.61mm \times 1864.3mm$ bars of extruded polystyrene scintillator, which are oriented perpendicular to the beam in either x or y direction. Each scintillator bar has a reflective coating containing TiO_2 and a WLS fiber going down a hole in its center. One end of each fiber is mirrored by vacuum deposition of aluminium, while the other end is attached to an Multi-Pixel Photon Counter (MPPC).
Each FGD (Figure 2.13) has outer dimensions of $2300mm \times 2400mm \times 365mm$ (width $\times$ height $\times$ depth in beam direction), and contains 1.1 tons of target material. The first FGD is composed by 5760 scintillator bars, arranged into 30 layers of 192 bars each, with

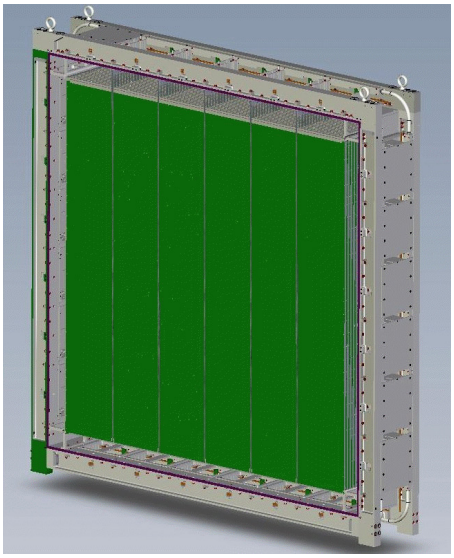

Figure 2.13: View of an FGD with the front cover removed.

each layer oriented in the x and y directions perpendicular to the neutrino beam. The second FGD is water-rich detector consisting of seven XY modules of plastic scintillator alternating with six 2.5 cm thick layers of water, in total we have 2688 scintillators bars and 15 cm thick of water.

2.3.6 Electromagnetic Calorimeter (ECAL)

The inner detector (composed of PØD,TPCs,FGDs) is surrounded by a sampling Electromagnetic Calorimeter (ECAL) for the detection of photons and measurement of their energy and direction, as well as the detection of charged particles and the extraction of information relevant to the particle identification. It uses layer of plastic scintillator bar ($4.0cm \times 1.0cm$ cross section) as active material with lead absorber sheets between layers, and it provides near-hermetic coverage for all particles exiting the inner detector volume.

The ECAL is made of 13 indipendent modules of three different types:

- six Barrel-ECAL surround the tracker volume on its four sides parallel to the beam direction;
- one downstream module (DsECAL) covers the downstream exit of the tracker volume;
- six PØD-ECAL modules surround the PØD, as the Barrel-ECAL does for the tracker volume.

Other 12 ECAL modules are mounted inside UA1 magnet.

2.3.7 UA1 magnet and Side Muon Range Detector (SMRD)

The ND280 uses the refurbished UA1/NOMAD magnet, that provide a dipole magnetic field of 0.2 T perpendicular to the neutrino beam direction, to measure the momentum with good resolution and determine the sign of the charge particles produced by neutrino interactions. The dimensions of inner volume of the magnet are $7.0m \times 3.5m \times 3.6m$ and the external ones are $7.6m \times 5.6m \times 6.1m$. The magnet consist of water-cooled aluminium coils, that operate at current of 3 kA, which create the horizontally oriented dipole field, and a flux return yoke. The coils are made of aluminium bars with $5.45cm \times 5.45cm$ square cross sections, with a central 23 mm diameter hole for water to flow. According to simulations the field is quite uniform in intensity and direction, with traverse components exceeding 1% only in regions close to the coils.

A total of 440 scintillator modules are located in the air gap between 4.8 cm thick steel plates, which make up the UA1 magnet flux return yokes. These scintillators compose the Side Muon Range Detector. Due to the differently sized spaces for horizontal and vertical gaps, horizontal modules consist of four scintillation counters and vertical modules consist of five scinitllation counters. The scintillation counters (Figure 2.14) are extruded polystyrene and dimethylacetamide with admixtures of POPOP and paraterphenyl. The surface of each scintillation counter features a white diffuse layer which acts as a reflector. A 1 mm diameter Kuraray Y11 double-clad wavelength shifter exits both sides of the scintillator through a ferrule which is part of an end-cap. The MPPCs are coupled to the polished WLS fiber ends through a snap-on mechanism. There are 4016 MPPCs connected to a miniature printed circuit (PCB). The miniature PCBs couple the MPPC signals into mini-coaxial cables, which lead the signal to the custom-designed Trip-T front-end boards (TFBs) mounted on the vertical sections of the magnet yokes.

The SMRD has three different goals:

- reject cosmic ray muons that enter or penetrate the ND280 detector from outside;
- detect muons escaping at large angles with respect to the beam direction and measure their momentum;
- help to identify beam-included interactions in the surrounding cavity walls and the iron of the magnet.

The average light yield of individual counters in response to a minimum ionizing particle amounts to about 50 photoelectons for the summed signal from both ends of a counter. The beam-related SMRD event rate of coincidence hits has been observed to be stable to within 3% after temperature corrections.

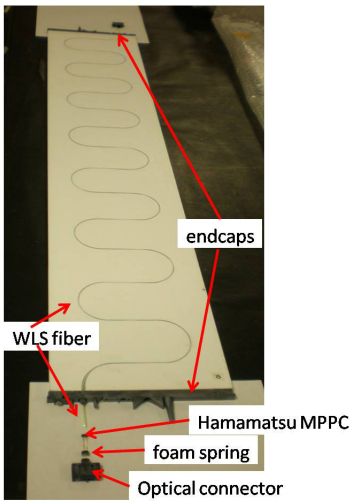

Figure 2.14: View of SMRD scintillation counter components prior to assembly.

2.4 Far detector: Super-Kamiokande (SK)

Super-Kamiokande (Figure 2.15) is a cylindrical 50 kton water Cherenkov detector located at Kamioka Observatory in Gifu Prefecture, 295 km away from J-PARC. It is located in an underground mine under the Ikenoyama mountain, at a mean depth of 1000 meters (equivalent to 2700 meters of water). The flux of cosmic rays is reduced by five orders of magnitudes compared to the one on the surface of the earth.

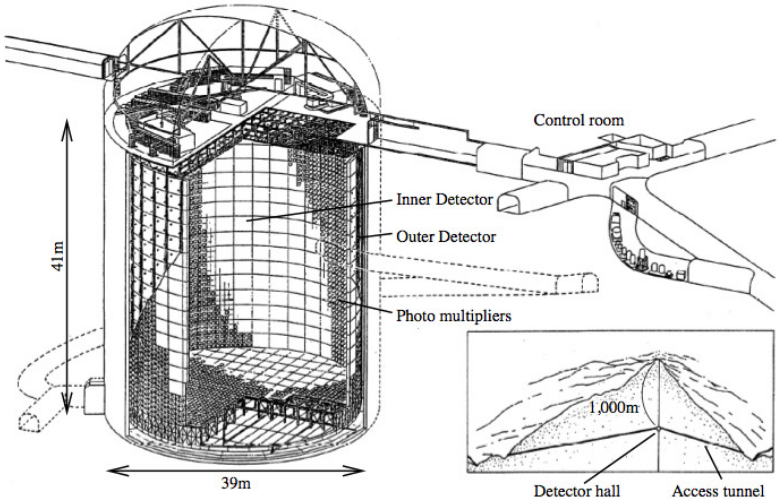

Figure 2.15: A view of the Super-Kamiokande detector.

The SK detector started taking data in April 1996, aiming for nucleon decay searches

and the study of atmospheric and solar neutrinos. The running period of the first five years is called SK-I. After it had been suspended for maintenance, an accident occurred in November 2001 and $\sim 60\%$ of the photomultipliers (PMTs) were broken. The detector was rebuilt with half of the PMTs in December 2002 and the running period after the accident is called SK-II. For the SK-III running period (2006-2008), the full complement of PMTs was restored, with original front-end electronics. The SK-IV running period (2008-2018) has the same PMT configuration as SK-III, but with completely updated, dead time-free data acquisition electronics.

On the SK walls roughly 13,000 photomultiplier tubes (PMTs) detect neutrino interactions. The SK detector structure is divided in two major volumes: an inner and an outer detector which are separated by a cylindrical stainless steel structure. The inner detector (ID) is a cylindrical space of 33.8 m in diameter and 36.2 m in height which currently houses along its inner walls 11129 inward-facing 50 cm diameter PMTs, providing 40% of surface coverage. The outer detector (OD) is a cylindrical space about 2 m thick radially and on the axis at both ends. The OD contains along its inner walls 1885 outward-facing 20 cm diameter PMTs and is used as an anti-counter to identify entering/exiting particles to/from the ID. The ID and OD boundaries are defined by a cylindrical structure about 50 cm wide. This structure consists of a stainless steel scaffold covered by plastic sheets which serve to optically separate the ID and OD. The wall facing into the ID is lined with a black sheet of plastic meant to absorb light and minimize the number of photons which either scatter off the ID wall back into the ID volume, or pass through from the ID to the OD.

The main role of Super-Kamiokande is to sample the beam's flavour composition and look for ν_e appearance and ν_μ disappearance. The primary strategy to measure the flavour composition of the T2K neutrino beam at SK, and thereby observe the oscillation of ν_μ to ν_e is to count CCQE interactions for muon and electron neutrinos, both of which produce leptons of their respective flavour. To reach this goal SK uses the Cherenkov effect of relativistic charged particles. The lepton, produced in these neutrino interactions, travels through the detector with a speed faster than the velocity of light in water. The polarized water molecules rapidly turn back to their ground state and emit Cherenkov light, which is detected by the ID PMTs. Not all charged particles produced in neutrino interactions are visible in SK because the Cherenkov effect has a energy threshold that depends on type of active material in the detector, in this case pure water, and on mass of particle that go through detector. In SK the threshold is equal to 775 keV for electrons, 160 MeV for muons and 1.4 GeV for protons. Given these thresholds and the energy of the T2K beam, the protons produced in neutrino interactions are usually below the Cherenkov threshold and are not detectable in Super-Kamiokande.

For both ν_μ and ν_e events the starting position of the leptons is required to be fully contained in the fiducial volume, which is defined to be more than 2 m away from the ID wall for a total fiducial mass of 22.5 kton. The pulse height and timing information of the

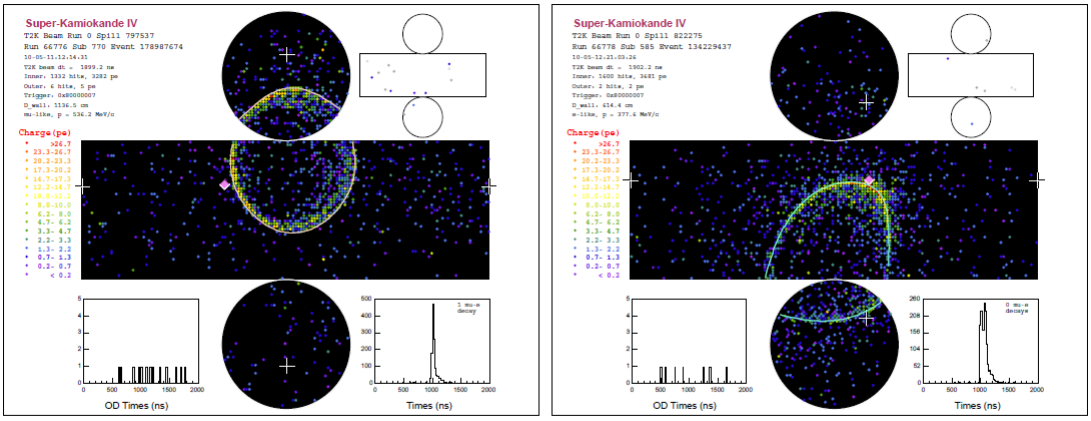

(a) muon-like event (b) electron-like event

Figure 2.16: Example of reconstructed T2K events in Super-Kamiokande for (a) a muon-like ring and (b) an electron-like ring. Both figures show the cylindrical detector unrolled onto plane. Each colored point represents a PMT, with the color corresponding to the amount of charge, and the reconstructed cone is shown as a white line.The second figure upper right corner shows the same hit map for the OD. The white crosses indicate the location of the reconstructed event vertex and heading in the direction of the beam would intersect the detector wall.

PMTs are fitted to reconstruct the vertex, direction, energy, and particle identification of the Cherenkov rings. A typical vertex, angular and energy resolution for 1 GeV muons is 30 cm, 3° and 3%, respectively. The typical ring shape of electrons and muons is a very good method to separate ν_μ from ν_e interactions (Figure 2.16).

The fuzzy electron like ring is due to the multiple scattering, which is more likely to occur for electrons than for muons because of the electron smaller mass, and to electromagnetic showers almost always induced at these energies. A typical rejection factor to separate muons from electrons (or vice versa) is about 100 for a single Cherenkov ring event at 1 GeV. The electrons and muons are further separated by detecting decay electrons from the μ decays. A typical detection efficiency of decay electrons from stopping cosmic muons is roughly 80%. A 4π coverage around the interaction vertex provides an efficient π^0 detection.

Chapter 3

Neutrino and anti-neutrino interactions

T2K has been designed to study of ν_e ($\bar{\nu}_e$) appearance and ν_μ ($\bar{\nu}_\mu$) disappearance in a (anti-)neutrino beam. In order to make high precision measurements it is fundamental to have an accurate knowledge of the neutrino and anti-neutrino cross sections. The cross section is an important information not only by itself but is vital for neutrino oscillation analysis. Indeed, neutrino oscillation experiments measure the number of CC events which is a convolution of the neutrino flux, cross-section and detector efficiency:

$$N(\vec{x}) = \Phi(E_\nu) \times \sigma_i(E_\nu, \vec{x}) \times \epsilon(\vec{x}) \times T_j \times P(\nu_\alpha \to \nu_\beta) \tag{3.1}$$

where $N(\vec{x})$ is the number of events as function of the kinematic of the outgoing particles, $\Phi(E_\nu)$ is the neutrino flux that depends on neutrino energy E_ν, $\sigma_i(E_\nu, \vec{x})$ is the cross section, $\epsilon(\vec{x})$ describes the detector response, T_j is the number of target nucleons and $P(\nu_\alpha \to \nu_\beta)$ is the oscillation probability.

3.1 Interactions with matter

In the Standard Model interactions occur between fermionic particles, that are divided in quark and leptons, through the exchange of gauge particles, which are bosons. Leptons and quarks can interact via weak and electromagnetic interaction, but only quarks interact also via strong interaction. The electromagnetic and strong interactions are mediated by massless vector gauge field, photon and gluons respectively, on the other hand the weak interaction is mediated by massive vector gauge bosons, Z^0 and $W^\pm$. In this description neutrinos have two possible types of weak interaction: via charged current (CC) interaction, where the neutrino is converted into lepton (or vice versa) through the bosons $W^\pm$, and via neutral current (NC) interaction where the neutrino exchanges the boson Z^0 with another particle only changing its energy.

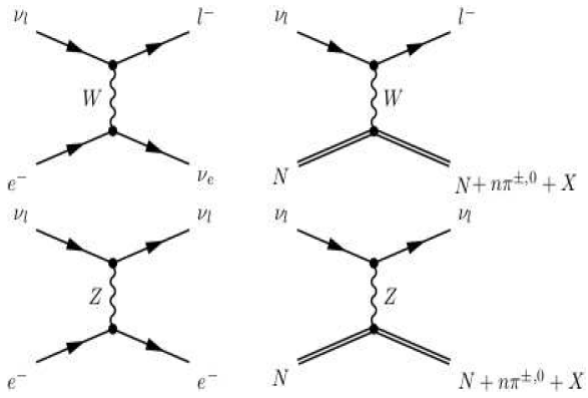

Figure 3.1: Feynman diagrams of neutrino interactions in matter in the case of charged and neutral current interactions. Analogue interactions hold for anti-neutrino.

Feynman diagrams of interactions between neutrinos and matter are shown in Figure 3.1. If we consider a massless muon neutrino that interact via CC with an atomic particle, the energy threshold in the laboratory frame is:

$$\begin{aligned} s &> M^2 \\ s = (p_{\nu_\mu} + p_i)^2 &= (E_{\nu_\mu} + m_i)^2 - E_{\nu_\mu}^2 \\ E_{\nu_\mu} &> \frac{M^2 - m_i^2}{2m_i} \end{aligned} \tag{3.2}$$

where M is the sum of final state mass particles, $p_{\nu_\mu} = (E_{\nu_\mu}, 0, 0, E_{\nu_\mu})$, s is the center-of-mass energy and the index i can be e^- or n for neutrinos interaction, and p for anti-neutrinos interaction. So we can find three different threshold energy:

$$\begin{aligned} E_{\nu_\mu} &> 11 \text{ GeV} \\ E_{\nu_\mu} &> 110 \text{ MeV} \\ E_{\bar{\nu}_\mu} &> 111 \text{ MeV} \end{aligned} \tag{3.3}$$

respectively for ν_μ interaction with electron and neutron, and $\bar{\nu}_\mu$ interaction with proton. For the neutral current interactions there is no threshold for any neutrino flavours and atomic particles.

3.2 Charged current neutrino-nucleon interaction

Since in T2K the beam energy peak is around 600 MeV, we can consider CC neutrino, or anti-neutrino, interactions only with nucleons:

$$\begin{aligned} \nu_\mu + N &\rightarrow \mu^- + X\ (CC) \\ \bar{\nu}_\mu + N &\rightarrow \mu^+ + X\ (CC) \\ \nu_\mu + N &\rightarrow \nu_\mu + X\ (NC) \\ \bar{\nu}_\mu + N &\rightarrow \bar{\nu}_\mu + X\ (NC) \end{aligned} \tag{3.4}$$

where N can be neutron or proton and X is the hadronic final state. Neutrino and anti-neutrino NC interactions are usually undetectable in water Cherenkov detectors because the outgoing protons do not have the energy to generate Cherenkov light, and the outgoing neutrons are undetectable. In order to improve the study of NC background at low energy, SK starts an upgrade project called SK Gadolinium Project is almost ready. The addition of the water-soluble gadolinium (Gd) salt provides the SK detector with the possibility to identify the neutrons coming from NC interaction [22]. As shown in Figure 3.2, at the energy of the T2K beam the CC inclusive cross-section of ν_μ and $\bar{\nu}_\mu$ are dominated by Charged Current Quasi-Elastic scattering (CCQE).

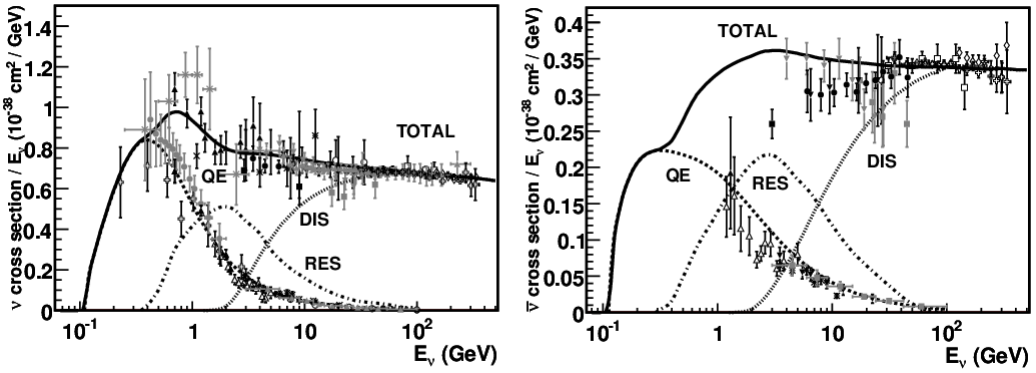

Figure 3.2: Muon neutrino (left) and antineutrino (right) CC cross-section measuraments and predictions as a function of neutrino energy.[16]

The linear rise of the cross-section with E_ν as observed in hard νN scattering is a direct evidence for scattering on point-like objects within the nucleon. This assumption is the basis of the quark-parton-model (QPM), which predicts that deep-inelastic νN scattering can be seen as an incoherent superposition of neutrino (anti-neutrino) quark scattering. Neutrino cross-sections are typically twice as large as their corresponding anti-neutrino counterparts, although this difference can be larger at lower energies. For $E_\nu < 30GeV$, the ratio $R = \frac{\sigma(\nu N)}{\sigma(\bar{\nu})N}$ can approach the simple QPM prediction without sea-quark contribution (R=3). The R is about 2 at higher energies and is a direct hint

for their contribution.

The associated differential cross-section as a function of the energy of the outgoing lepton E_l and its angle with respect to the incoming neutrino θ_l, can be expressed as follows:

$$\frac{d^2\sigma}{dE_l d\cos\theta_l} = \frac{1}{32\pi^2 m_N}\frac{|\vec{p_l}|}{E_\nu}|\mathcal{M}|^2 \prod_X \frac{d^3\vec{p_X}}{(2\pi)^3 2E_X}(2\pi)^4\delta^4\left(\sum_X p_X - p_l - p_N - p_\nu\right) \quad (3.5)$$

with $\mathcal{M}$ invariant matrix element that, in the Born approximation, for neutrino CC interactions can be written as:

$$\mathcal{M} = \left(\frac{g}{2\sqrt{2}}\right)^2 \bar{l_L}(k^{'})\gamma_\alpha(1-\gamma_5)\nu_L(k)\frac{i}{q^2 - M_W^2}\left(-g_{\alpha\beta} + \frac{q^\alpha q^\beta}{M_W^2}\right)\langle X(p^{'})|j_\beta|N(p)\rangle \quad (3.6)$$

If the square of the four-momentum transfer to the nucleon is much smaller than the intermediate vector boson mass squared, then the spin averaged matrix element is given by

$$|\mathcal{M}|^2 = \frac{G_F}{2}L_{\alpha\beta}W^{\alpha\beta} \quad (3.7)$$

with

$$\frac{G_F}{\sqrt{2}} = \frac{g^2}{8M_W^2} \quad (3.8)$$

where $L_{\alpha\beta}$ and $W^{\alpha\beta}$ are the leptonic and hadronic tensor respectively. Then the cross-section is given by:

$$\frac{d^2\sigma}{dE_l d\Omega_l} = \frac{G_F^2}{4\pi^2}\frac{|\vec{k}|}{|\vec{k'}|}L_{\alpha\beta}W^{\alpha\beta}d\Omega_l = d\Omega_l \quad (3.9)$$

The leptonic tensor can be written as:

$$L_{\alpha\beta} = k_\alpha k^{'}_\beta + k^{'}_\alpha k_\beta - g_{\alpha\beta}k\cdot k^{'} \pm i\epsilon_{\alpha\beta\sigma\delta}k^{'\sigma}k^\delta \quad (3.10)$$

where $g_{\alpha\beta}$ is the Minkowski metric matrix and the convention for the fully anti-symmetric Levi-Civita tensor is $\epsilon_{0123} = +1$. The + in eq. 3.10 is valid for ν while - for $\bar{\nu}$ interactions. The hadronic tensor, representing the structure of the nucleon, is completely determined by six independent structure functions [31]:

$$W^{\alpha\beta} = -g^{\alpha\beta}W_1 + \frac{p^\alpha p^\beta}{M^2}W_2 + \frac{i\epsilon^{\alpha\beta\rho\sigma}p_\rho p_\sigma}{2M^2}W_3 + \frac{q^\alpha q^\beta}{M^2}W_4 + \frac{p^\alpha q^\beta - q^\alpha p^\beta}{M^2}W_5 + \frac{i(p^\alpha q^\beta - q^\alpha p^\beta)}{M^2}W_6 \quad (3.11)$$

The function W_i are real function of $\nu = p\cdot q$ and the square momentum transferred $Q^2 = -q^2$. So the double differential cross section of CC neutrino, or anti-neutrino,

cross-section is written as:

$$\begin{aligned}\frac{d^2\sigma}{dE_l d\Omega_l} = \frac{|\vec{k'}|E_l M G_F^2}{\pi^2}\{2W_1 \sin^2\frac{\theta_l}{2} + W_2\cos^2\frac{\theta_l}{2} \mp W_3\frac{E_\nu + E_l}{M}\sin^2\frac{\theta_l}{2} \\ + \frac{m_l^2}{E_l(E_l+|\vec{k'}|)}[W_1\cos\theta_l - \frac{W_2}{2}\cos\theta_l \pm \frac{W_3}{2}\left(\frac{E_l+|\vec{k'}|}{M} - \frac{E_\nu+E_l}{M}\cos\theta_l\right) \\ + \frac{W_4}{2}\left(\frac{m_l^2}{M^2}\cos\theta_l + \frac{2E_l(E_l+|\vec{k'}|)}{M^2}\sin^2\theta_l\right) - W_5\frac{E_l+|\vec{k'}|}{2M}]\}\end{aligned} \tag{3.12}$$

where the terms proportional to W_6 do not survive to the tensors contraction, the second sign is for anti-neutrino cross-section, M is the mass of nucleon, θ_l is the scattering angle of the outgoing lepton, $\vec{k'}$ is its momentum and $E_{\nu(l)}$ is the neutrino (lepton) energy [29].

3.2.1 Quasi Elastic Charged Current scattering

The neutrino and anti-neutrino CCQE nucleon scattering are the dominant reactions at T2K beam energy. This type of reaction is represented as interaction between neutrino/anti-neutrino with a free nucleon (Impulse Approximation):

$$\begin{aligned}\nu_l + n &\to l^- + p \\ \bar{\nu}_l + p &\to l^+ + n\end{aligned} \tag{3.13}$$

Between 1970's and 90's this reaction was used to study the V-A nature of the weak interactions and to measure the axial-vector form factor of the nucleon. These experiments used deuterium-filled bubble chambers. Since CCQE is a two body interaction, the neutrino energy can be completely reconstructed from the kinematic of the outgoing lepton. In fact if the target nucleon is at rest (we can consider the nucleon target at rest if E_ν is large enough) we can write:

$$E_\nu = \frac{m_n E_l + \frac{1}{2}\left(m_p^2 - m_n^2 - m_l^2\right)}{m_n - E_l + p_l\cos\theta_l} \tag{3.14}$$

with p_l and θ_l the momentum and the angle of the outgoing lepton with respect to the neutrino direction.

The CCQE differential cross-section can be expressed as [16]:

$$\frac{d\sigma}{dQ^2} = \frac{G_F^2 M^2 |V_{ud}|^2}{8\pi E_\nu^2}\left[A(Q^2) \pm \frac{(s-u)}{M^2}B(Q^2) + \frac{(s-u)^2}{M^4}C(Q^2)\right] \tag{3.15}$$

where $\pm$ refers to neutrino/anti-neutrino interaction, s and u are the Mandelstam variables ($s - u = 4ME_\nu - Q^2 - m_l^2$, with m_l lepton mass) and $|V_{ud}|^2$ term is the element of

the CKM (Cabibbo-Kobayashi-Maskawa) matrix. The factors $A(Q^2), B(Q^2)$ and $C(Q^2)$ are form factors of the nucleon:

$$\begin{aligned} A(Q^2) = \frac{m_l^2 + Q^2}{M^2}[(1+\eta)F_A^2 - (1-\eta)F_1^2 + \eta(1-\eta)F_2^2 \\ +4\eta F_1 F_2 - \frac{m^2}{4M^2}((F_1+F_2)^2 \\ + \left(F_A + 2F_p)^2 - \left(\frac{Q^2}{M^2} + 4\right) F_p^2\right)] \end{aligned} \tag{3.16}$$

$$B(Q^2) = \frac{Q^2}{M^2} F_A (F_1 + F_2) \tag{3.17}$$

$$C(Q^2) = \frac{1}{4}(F_A^2 + F_1^2 + \eta F_2^2) \tag{3.18}$$

where $\eta = \dfrac{Q^2}{4M^2}$, F_1 and F_2 are the vector form factors and F_A is the axial form factor of the nucleon. This formalism was used to analyse neutrino quasi-elastic scattering data on deuterium. It is important to note that $B(Q^2)$ contains the interference between the axial and vector currents, and it is responsible for the Q^2 dependent difference between ν and $\bar{\nu}$ cross-sections. In the conserved vector current (CVC) hypothesis, the vector form factors could be obtained from electron scattering, thus leaving the neutrino experiments to measure the axial-vector form factor of the nucleon. In the approximation of Dipole Form Factors, the axial form factor is given by:

$$F_A(Q^2) = \frac{g_A}{\left(1 + \dfrac{Q^2}{M_A^2}\right)^2} \tag{3.19}$$

which depends on two empirical parameters: the value of the axial-vector form factor at $Q^2 = 0$, $g_A = F_A(0) = 1.2694 \pm 0.0028$ [26], and an "axial mass", $M_A = 1.026 \pm 0.021$GeV. This value has been obtained from global fit to the deuterium data [12]. Currently experiments do not use deuterium as neutrino target but use complex nuclei so nuclear effects became much more important and produce modifications to QE differential cross-section. In fact the value of M_A is significantly different ($M_A = 0.999 \pm 0.011$ GeV [21]) if heavy target data are added.

3.2.2 Resonant production

The resonant channel can be accessed when the center of mass energy of a neutrino-nucleon interaction exceeds the mass of a resonant baryon particle. Neutrino and anti-neutrino Charged Current Resonant Channel (CC RES) processes are:

$$\nu(\bar{\nu}) + N \rightarrow l^-(l^+) + res \rightarrow l^-(l^+) + N' + meson(s) \tag{3.20}$$

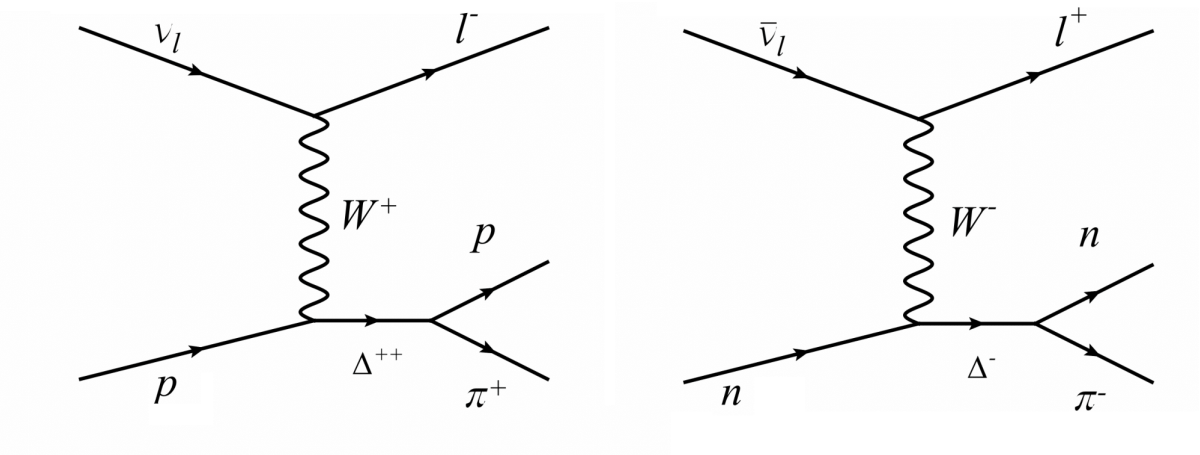

Figure 3.3: Feynman diagram of one of possible CC RES neutrino (left) and anti-neutrino (right) interaction.

where N is proton or neutron, $l^{\pm}$ a lepton and *res* is a baryon resonant particle, that can be Δ^{++} or Δ^{-} as shown in Figure 3.3. These resonances then decay to a nucleon, most often accompanied by a single pion. However a variety of final-states can result depending on the resonance and can include multiple pions, kaons or radiative photons.

The most common result of resonance decay is single pion production, usually estimated for neutrino experiments following the Rein and Sehgal model [28] with the additional inclusion of lepton mass terms. Resonance production is most significant in the transition region $0.5\,\text{GeV} < E_\nu < 10\,\text{GeV}$ and it is a background for neutrino oscillation experiments searching for ν_e, since the signal produced by $\pi^0 \to 2\gamma$ can easily mimic an electron.

3.2.3 Deep inelastic scattering

Deep Inelastic Scattering (DIS) is the dominant interaction at the neutrino energies of the order of several GeV or higher. At these energies neutrino resolve the individual quarks in the nucleon, then the knocked quarks give rise to an hadronization where a jet of particles is produced. This scattering can be described by:

$$\begin{aligned} \nu + N &\to l^- + X \\ \bar{\nu} + N &\to l^+ + X \end{aligned} \tag{3.21}$$

with N=p,n and X a hadronic system. For high energies it is necessary to describe the interaction as a reaction between neutrino and partons inside nucleons. As for CCQE scattering, also in DIS the nuclear environment has to be approximated to *Relativistic Fermi Gas* (RFG), assuming that nucleons are quasi-free.

3.3 Charged current neutrino-nucleus interaction

Theoretical modelling of the neutrino-nucleus scattering face many complications. The first is the representation of initial state of the nucleons inside the nucleus. The simplest approximation is the RFG that considers each nucleon quasi-free. This works out well for old experiments, that used deuterium as target, but experiments like MiniBooNE and NOMAD (that used carbon target) did not measure the expected CCQE cross-section. It is currently believed that nuclear effects beyond the impulse approximation approach are responsible for the discrepancies observed in the experimental data. An additional complication is that the neutrino can interact not only with individual nucleons, but the interaction can include correlated nucleon pairs or any combination of nucleons in quasi-bound state. The particle produced in the neutrino interaction have to propagate out through the nucleus, where they can interact with other nucleons. These processes, called "final-state interaction" (FSI), can alter the particles type and number (Figure 3.4). The nucleon-nucleon correlations and two-body exchange currents must be included in order to provide a more accurate description of neutrino-nucleus QE scattering [16].

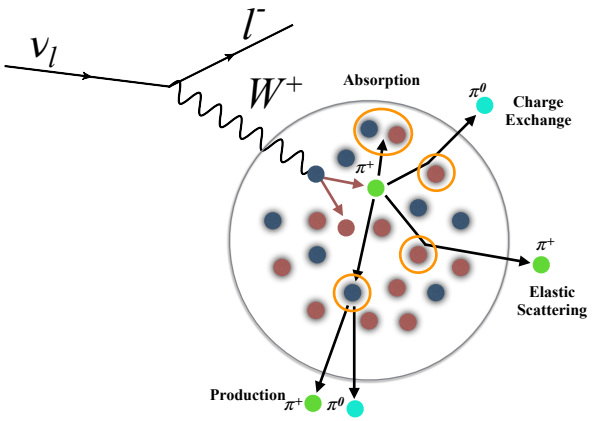

Figure 3.4: Representation of the possible pion FSI interaction in the nuclear matter [29].

If we consider CC inclusive neutrino-nucleus scattering, the cross-section has the same expression of the neutrino-nucleon cross-section. The only difference is in the hadronic tensor, that can be written as:

$$W^{\alpha\beta} = W_s^{\alpha\beta} + iW_a^{\alpha\beta} \tag{3.22}$$

with $W_s(W_a)$ the symmetric (antisymmetric) tensor. It can be expressed in terms of the polarization propagator

$$W_{(s,a)}^{\alpha\beta} = -\frac{1}{\pi}\Pi_{(s,a)}^{\alpha\beta} \tag{3.23}$$

This is a result obtained for the response of many-body systems to external probes [15], different nuclear models create different expressions for the polarization propagator. The models typically used to described this effect are: *Relativistic global Fermi Gas (RFG)*, *Relativistic local Fermi Gas (LFG)* and *Spectral Function (SF)*. The formalism introduced for CCQE, CC RES and DIS channels is still valid for neutrino-nucleus scattering, but other channels have to been added to the neutrino-nucleon interaction: the so-called multi-nucleon knock-out and the coherent pion production (COH).

3.3.1 Multi-nucleon knock-out

The multi-nucleon knock-out reaction was firstly introduced as solution to ν_μ CCQE cross-section on carbon measurement problem of MiniBooNE [8]. This experiment reported a cross-section per nucleon $\sim$ 20% higher than expected from bubble chamber data. Initially the MiniBooNE analysis took also into account the possibility that in the neutrino interaction, a pion produced via RES escapes detection simulating a CCQE process. The size of the cross-section was found to be well described by the RFG model with an axial mass of $M_A = 1.35 \pm 0.17 GeV/c^2$, which is in contradiction not only with the bubble chambers results, but also with NOMAD data, that found $M_A = 1.05 \pm 0.06\, GeV/c^2$ [24]. A possible solution to this "CCQE puzzle" was proposed by Martini et al.[25] by considering the multi-nucleon knock-out interaction. The interaction with a single nucleon which is knocked-out (the true CCQE event) is not the only one possible. In addition one must consider the interaction with a correlated pair of nucleons (NN correlations) that lead to two nucleon excitation (2p-2h) as schematically represented in Figure 3.5.

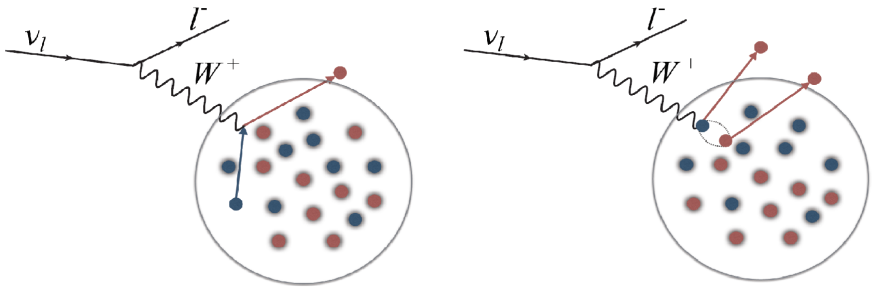

Figure 3.5: Schematic representation of a genuine CCQE (left) and a 2p2h (right) process [29].

3.3.2 Coherent Scattering (COH)

In addition to the 2p2h process, neutrino can also coherently scatter off the entire nucleus and produce a distinctly forward-scattered single pion final state, leaving the nucleus

in the same state as before neutrino scattering. This can only be achieved if the 4-momentum transfer to the nucleus is kept small. The COH process can occur in both neutral current interactions and charged current interactions:

$$\begin{aligned} \nu(\bar{\nu}) + A \rightarrow \nu(\bar{\nu}) + \pi^0 + A \ \ (NC) \\ \nu(\bar{\nu}) + A \rightarrow l^-(l^+) + \pi^+(\pi^-) + A \ \ (CC) \end{aligned} \tag{3.24}$$

where A is the unchanged target nucleus. It is important to study this processes because they are a source of neutral pions, that are the main backgrounds to the ν_e appearance measurement.

3.4 Significant processes for T2K experiment

The main interaction channels at the energies of T2K are:

- Charged-current quasi-elastic scattering;
- Charged-current resonant pion production;
- Charged-current deep inelastic scattering;

As shown in Figure 3.6, CCQE interactions are the most relevant around 1 GeV. The reconstruction of the incoming (anti-)neutrino energy is performed using the Eq. 3.14. Until recently, oscillation analyses of T2K data divided the charged current inclusive sample into two: CCQE-like and the rest. However, considering the FSI problem, a new type of division of CC inclusive sample is made, defined by the number of the final state pions: zero pions($CC0\pi - like$), one positive pion ($CC1\pi^+ - like$), and any other combination of type and number of pions ($CCOther - like$). This categories have enhanced ability to constrain the CCQE and RES single pion cross-section parameters reducing the uncertainties on the oscillation analyses [1]. These processes affect the efficiency of pion identification and the rate of π^0 production, which is an important background for ν_e appearance measurement. So the interaction of a neutrino with a nucleus add more channels compared to the neutrino-nucleon interaction.

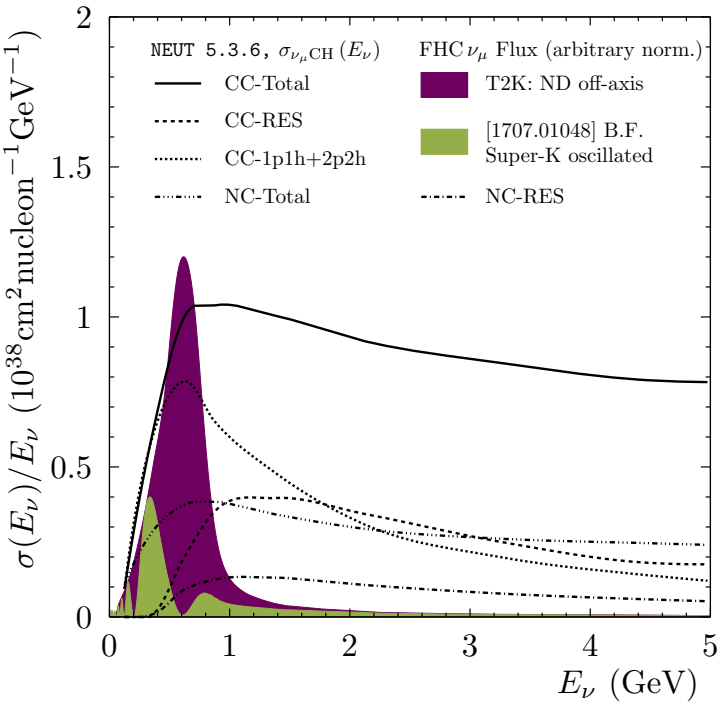

Figure 3.6: Main interaction channels at T2K overlaid with expected ND280 and SK fluxes.

Chapter 4

Muon anti-neutrino charged current event selection

4.1 Motivations and objective

The main role of ND280 is to measure the flux and cross-sections reducing the systematics errors in T2K oscillation analyses. Such measurements are performed fitting a sample of CC-Inclusive interactions with vertex in one of the FGDs. So far, the selection of CC events has been limited only to the forward-going (w.r.t beam direction) muons. Anyway, the events at SK, given the symmetry of the detector, are selected in all the solid angle. The expected distributions of the lepton scattering angle ($\cos\theta$) for the $\nu_e(\bar{\nu}_e)$ and $\nu_\mu(\bar{\nu}_\mu)$ (Figure 4.1) events in SK show that in the ν_e appearance and ν_μ disappearance analyses the presence of backward-going track. The effect is less evident in the ν_μ analysis than

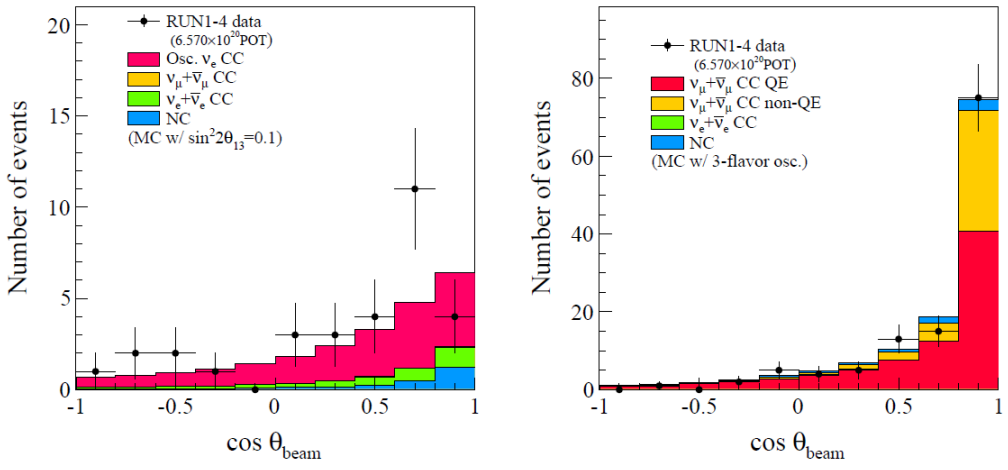

Figure 4.1: Distribution of the cosine of the angle between the reconstructed ring direction and the beam direction in the event selected at SK for the ν_e appearance (left) and ν_μ disappearance (right) analysis.

in the ν_e analysis, since there is no cut on the reconstructed energy and the backward events tend to have smaller momenta. Also in the ν_μ sample a non negligible amount of leptons are produced backward. Although for anti-neutrinos the cross-section suppress the backward-going leptons, for the aforementioned reasons, it is still crucial to study the lepton scattered at high angle.

In order to improve the measure of the flux and cross-section parameters, and so of the oscillation parameters, the Collaboration began to improve the selection of CC events in order to select events going backward or high-angle w.r.t. the neutrino direction. The selected samples can also be used to measure (anti-)neutrino cross-sections with a 4π coverage. The work of this thesis focused on the selection of a sample of $\bar{\nu}_\mu$ CC-Inclusive interactions (CC-Inclusive sample) in FGD1 in all the solid angle.

4.2 Data sets

The $\bar{\nu}_\mu$ selection in the anti-neutrino beam has been performed with the data taken from May 2014 to May 2016 which correspond to an exposure of 6.2×10^{20} protons on target (POT) collected at ND280 during three physics runs as detailed in Tab. 4.1. The samples used for the optimization of the selection are produced by Monte Carlo (MC) generator NEUT version 5.3.2. MC interactions within ND280 magnet and outside ND280 (called "sand muon") were generated separately. All the MC samples are normalized to the data POT.

Sample	Data POT (10^{20})	MC POT (10^{20})	MC SAND POT(10^{20})
Run5	0.4	23.0	4.3
Run6	3.4	9.9	4.3
Run7	2.4	33.7	4.3
Total	6.2	66.6	12.9

Table 4.1: Number of POTs for each data set and Monte Carlo simulation.

4.3 Analysis parameters definition

In order to optimize the selection, we have defined two parameters: the purity and the efficiency. The ***Purity*** (ρ) is defined as:

$$\rho = \frac{CCSignal}{CCSignal + Backgrounds} \tag{4.1}$$

where *CCSignal* is the number of $\bar{\nu}_\mu$ CC-Inclusive selected events and *Backgorunds* is the number of all the other events with the same reconstructed features. This parameter indicates how much the selected sample is actually made up of only the events we

are looking for. We assume the number of events is distributed as a poisson distribution, because these variables are associated to some counts. So for the rules of errors propagation, we can write the error on ρ as:

$$\sigma_\rho = \frac{\sqrt{CCSignal \cdot Backgrounds(CCSignal + Backgrounds)}}{(CCSignal + Backgrounds)^2} \tag{4.2}$$

The other parameter is the ***Efficiency*** (ϵ):

$$\epsilon = \frac{trueCCSignal}{trueCCevents} \tag{4.3}$$

with *trueCCSignal* the number of the true $\bar{\nu}_\mu$ charged current events which have passed the cut, and *tureCCevents* the number of the true $\bar{\nu}_\mu$ charged current events which we have before cut. The error of ϵ is measured as:

$$\sigma_\epsilon = \sqrt{\frac{\epsilon(1-\epsilon)}{trueCCevents}} \tag{4.4}$$

The goal of this work is to build a selection with high purity and, at the same time, high efficiency. In order to reach this purpose, we define another parameter (η) as product of ϵ and ρ. The choice of the values to be used in the cuts is made by maximizing such parameter. In the case of two or more different cuts have the same η value, we take the configuration with higher purity. The error on η (σ_η) is measured by:

$$\sigma_\eta = \sqrt{\rho^2\sigma_\epsilon^2 + \epsilon^2\sigma_\rho^2} \tag{4.5}$$

4.4 Previous $\bar{\nu}_\mu$ selection

Before describing the improved $\bar{\nu}_\mu$ CC-Inclusive selection, we look in details the steps employed in the previous selection to understand which of these can be improved or removed. The main focus of the previous selection was to collect the interaction which produces positive muon with more than 19 hits in TPC2, so this selection collected only forward-going events. In order to reach this goal the experiment used the steps shown in Tab 4.2 and detailed below:

- **Event quality**: the anti-neutrino beam is produced spilling 8 proton bunches from Main Ring, which have a width of 15 ns, and they collide on a graphite target as described in chapter 2. Only events associated to beam trigger and compatible with one of the eight bunches are selected. To do this selection the mean and the width of each bunch are measured and only the tracks produced in a time window of four times the width of bunch are accepted.

- **Total multiplicity**: only the events that have at least one reconstructed track in TPC2 are accepted. In order to consider a good TPC reconstructed track, the

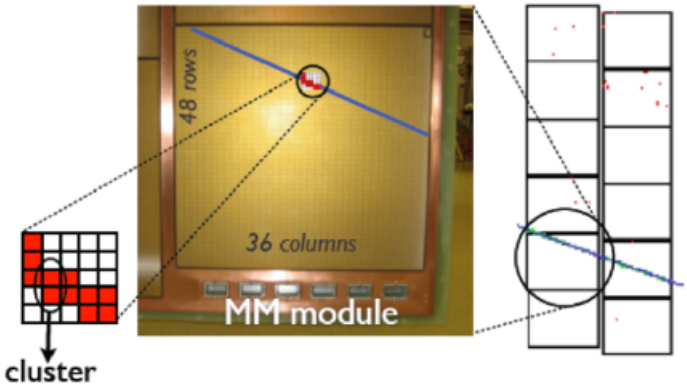

Figure 4.2: A schematic view of a cluster in a TPC.

particle has to leave at least 19 clusters at TPC2. A cluster, or hit, is defined as a contiguous illuminated pad in a row or column in the same micromegas (Figure 4.2). 19 is the minimum number of hits that we need to make a good TPC particle identification with the likelihood method.

- **Fiducial Volume (FV)**: an event is selected if the reconstructed vertex of a $\bar{\nu}_\mu$ interaction is inside FGD1 fiducial volume. The Highest Momentum Positive Track (HMPT) is considered as μ^+ candidate, and its starting position is used to define the interaction vertex position. The starting point is defined by the intersection of the fitted positive muon track and the XY plane at the Z position of the most upstream FGD1 hit of the track. For tracks emitted at high angle with respect to the beam direction, the reconstructed algorithm can use the XZ or YZ planes located at the first FGD1 hit. The idea is to reduce the rate of event with vertex outside the FGD1 but with a reconstructed track starting inside it. Cuts in x and y direction accept only those interactions within 5 bars from the edge of the XY modules of FGD1. The FV in z direction excludes the first most upstream module and include all the remaining modules of FGD1.

- **Positive multiplicity**: the HMPT, which has the starting vertex in FGD1 FV, must be also the Highest Momentum Track (HMT) of the event. This cut reduce the contribution of the CC-RES ν_μ interaction.

- **Upstream background veto**: reconstruction failures can lead to a positive muon track starting form FGD1 FV even if the real positive muon started far upstream. In order to exclude this type of events, we see the difference of the second highest momentum track start position and the start position of the positive muon candidate. If these two positions are too close the event is rejected.

- **Broken track**: this cut is applied to reject events with mis-reconstructed tracks,

where instead of one positive muon candidate track originated in FGD1 FV, the reconstruction breaks this track into two components: one fully contained FGD track (FGD-only track) followed by second track which starts in the last layers of FGD and passes TPC. In this kind of events the second track is considered as positive muon candidate. Thus the event with an FGD-only track and with the start position of an positive muon candidate in the last two scintillator layers of the FGD are rejected.

- **TPC particle identification (PID)**: so far the selected event was composed of positive tracks, now we analyse the energy loss in the TPC to understand if they are actually μ^+. In order to do a particle identification, we create a pull as:

$$\delta(i) = \frac{C_T^{meas} - C_T^{exp}(i)}{\sigma_i^{exp}} \tag{4.6}$$

where $i = (\mu, \pi, p, e)$, $C_T^{exp}(i)$ is the expected mean of energy deposit under the assumption of a particle type i and σ_i^{exp} is the deposit energy resolution. The pulls is computed for each TPC segment of the track (e.g., if the track crosses only the TPC2 one δ_i is computed, if the tracks goes through two TPCs two value of pulls are computed). Using these pull distributions, we define the likelihood as:

$$\mathcal{L}_i = \frac{\mathcal{P}_i}{\mathcal{P}_\mu + \mathcal{P}_e + \mathcal{P}_p + \mathcal{P}_\pi} \quad i = (\mu, \pi, e, p) \tag{4.7}$$

with the probability density function:

$$\mathcal{P}_i = \frac{1}{\sqrt{2\pi}\sigma(i)} exp\left(- \sum_j^{TPC_j} \frac{\delta_j^2(i)}{2} \right) \quad i = (\mu, \pi, e, p) \tag{4.8}$$

where j indicates the j-th TPC segment contained in the track. If positive muons are selected correctly, the δ_μ distribution obtained will be a Gaussian centered in zero with a sigma around one. On the contrary, if the track is not a positive muon, the difference between the measured energy loss and the expected one will be bigger and there will be a change in the pull distribution shape.
The TPC PID in this analysis is performed using the muon and MIP likelihoods, where the second is defined in the following way:

$$\mathcal{L}_{MIP} = \frac{\mathcal{L}_\mu + \mathcal{L}_\pi}{1 - \mathcal{L}_p} \tag{4.9}$$

The cuts on such variables were the following:

$$\begin{aligned} 0.1 \; < \; \mathcal{L}_\mu \; < \; 0.7 \\ \mathcal{L}_{MIP} \; > \; 0.9 \, for \, p \; < \; 500 \, MeV/c \end{aligned} \tag{4.10}$$

Cut name	Cut description
Event quality	The event must occur in defined bunch.
Total multiplicity and quality	The event has at least one reconstructed track in TPC2.
Fiducial Volume	The HMPTin the event must have its origin in FGD1 FV.
Positive multiplicity	The HMPT must be also the HMT in the event.
Upstream background veto	Veto tracks originated outside of the FGD1 FV.
Broken track	Rejection of external background from the last two layers of FGD1.
TPC PID	μ^+ identification using the TPC PID: $\mathcal{L}_\mu$ and $\mathcal{L}_{MIP}$.

Table 4.2: Summary table of the selection criteria applied in the previous $\bar{\nu}_\mu$ analysis.

4.5 Improved $\bar{\nu}_\mu$ CC-Inclusive selection

The aim of this work is to include to the sample all charged current events without a direction constrain. The idea behind this selection is to divide the total sample in four parts: *Forward (FWD)*, *Backward (BWD)*, *High angle Forward (HAFWD)* and *High angle Backward (HABWD)*. They will be analysed individually, using different cuts for each sample. In the Table 4.3 are summarized the various steps of the selection we have performed.

Step number	Step name			
	Forward	*Backward*	*HAForward*	*HABackward*
Cut 1	Event quality			
Cut 2	Total multiplicity			
Cut 3	TPC sorting			
Cut 4	Good quality and Fiducial			
Cut 5	FGD1 layer cut			
Cut 6	Upstream veto			
Cut 7	TPC PID FGD2 PID ECAL PID	TPC PID	ECAL PID	ECAL PID

Table 4.3: Summary table of the selection criteria applied in the improved $\bar{\nu}_\mu$ analysis.

We start applying two cuts:

- **Event quality**: this cut is the same of the one used in the previous selection (see 4.3).

- **Multiplicity cut**: we select only events which have at least one reconstructed track going through FGD1. Even if the name is the same as the cut in the previous selection, this one is totally different. In fact we want to include events with tracks that have less then 19 hits in TPCs or that do not go through TPCs, so we cannot use the information on TPCs hits for this cut.

After these cuts we define as a main track the positive track with the highest momentum. The number of hits of the main track in the TPCs is used to sort the events in CC sample into two new samples (**TPC sorting**): *Low Angle (LA)* sample, where we collect the events that have main track with more than 18 hits in TPC1 or TPC2, and *High Angle (HA)* sample where there are the events with main track with less than 19 hits. On the average, it also means to separate events in which the main track scattering angle (θ) is low from those events with high θ. To understand better this division we can see the Figure 4.3.

As in the previous selection, we apply the **Good quality and Fiducial** cut, where we

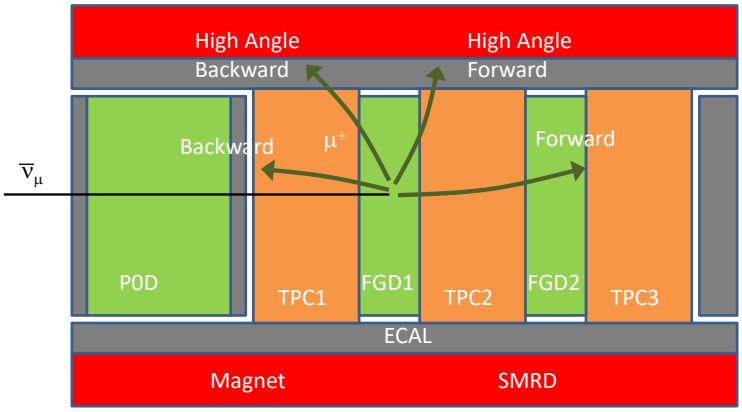

Figure 4.3: Schematic view of the events direction.

require the vertex to be inside the defined FGD1 FV (Figure 4.4) that, in this case, is all FGD1 excluded the last 5 layers in the direction x and y.

In addition, in this selection step, the propagation direction of the main track is also observed, so that the four samples seen previously can be constructed. To do this we use the Time of Flight (ToF) of the positive muon candidate between two sub-detectors of ND280. In order to separate forward-going (meaning $z_{start} < z_{end}$) and backward-going (meaning $z_{start} > z_{end}$) tracks in LA and HA sample is possible to utilize different ToF information; in fact for LA sample we use the ToF between FGD1 and FGD2, FGD1 and PØD. For the HA sample we can use only the ToF between FGD1 and Barrel ECal.
After these three general cuts the sample is composed as described in Table 4.4.

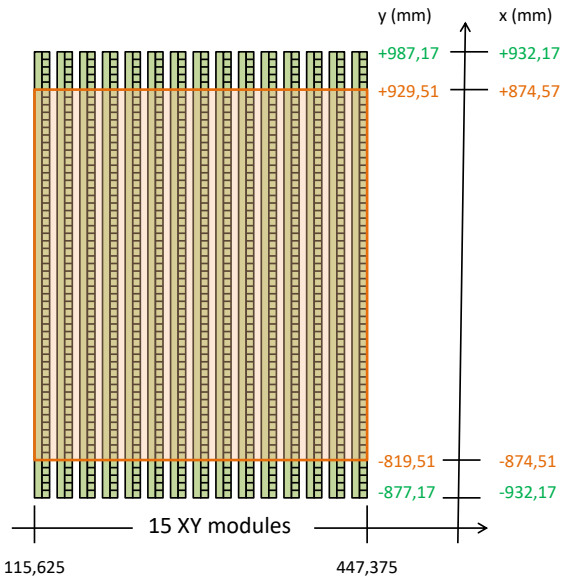

Figure 4.4: FGD1 scheme. Orange box indicate the fiducial volume.

	Fraction(%)
True reaction	Sample
$\bar{\nu}_\mu$CC-inclusive	26.9
ν_μCC-inclusive	11.8
NC, ν_e,$\bar{\nu}_e$	9.9
Out of FGD1 FV	49.0
sand μ	2.4

	Fraction(%)
Particle	CC sample
μ^+	38.7
π^+	10.7
e^+	9.2
μ^-	2.7
π^-	1.1
e^-	7.1
p	27.8
Other	0.4
sand μ	2.4

Table 4.4: Composition in particle and reaction of the sample after first three cuts.

4.6 Forward selection

The forward selection (FWD) is similar to the previous $\bar{\nu}_\mu$ selection with some addition and some new optimization. In the following, a detailed explanation of the selection criteria and analysis is shown.

4.6.1 FGD1 layer cut

At this point we have a sample composed of only events with the highest momentum positive charged low angle track starting in the FGD1 FV and it must have forward direction. Now we analyse the vertex position in the FGD1. As show in Figure 4.5,

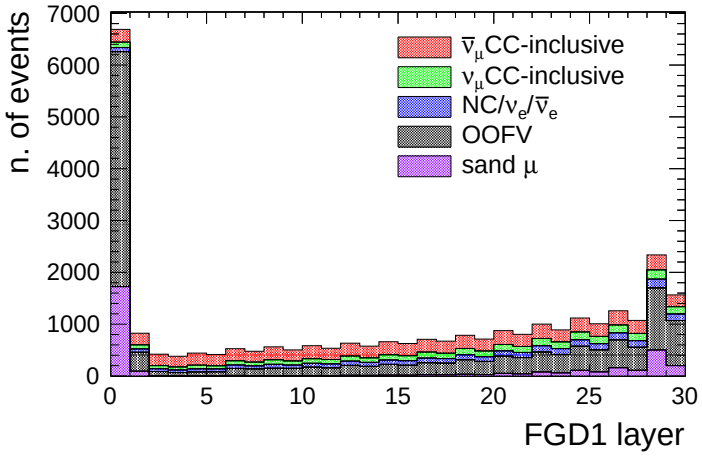

Figure 4.5: Start layer in FGD1 of the highest momentum positive charged low angle track with forward direction. Colours indicate different topologies of interaction.

the main backgrounds are Out Of Fiducial Volume (OOFV) events and sand muon. In order to reduce this background, the best choice is to exclude all the events with the reconstructed vertex in the first layer and last two layers. The results of the analysis is summarized in Table 4.5.

Excluded layer	$\rho(\%)$	$\epsilon(\%)$	$\eta(\%)$
0	32.3	96.6	31.2
0-1	32.4	93.5	30.3
0-29	33.4	93.5	31.2
0-1-29	33.6	90.3	30.3
0-28-29	35.4	89.5	31.7
0-1-28-29	35.6	86.3	30.8

Table 4.5: Results of the FGD1 vertex cut analysis for the FWD sample. The error for all the results is 0.1%.

4.6.2 Upstream veto cut

The idea of the cut is the same as that of the previous $\bar{\nu}_\mu$ selection. We want to reject events where the reconstruction can break a single track into two pieces, and one of those

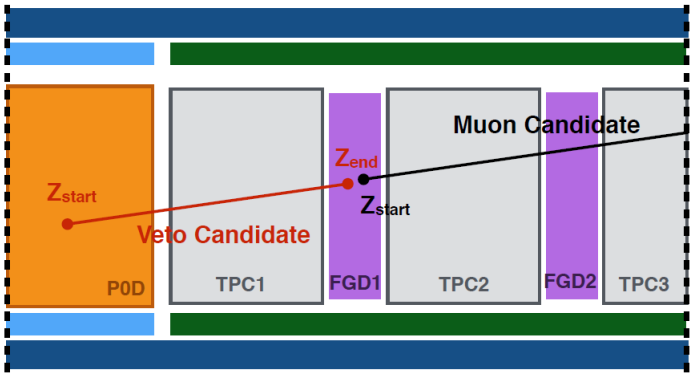

Figure 4.6: Schematic view of the tracks that will be rejected by the veto cut.

can have the starting vertex in the FGD1 FV even if the true track was originated outside the fiducial volume (see Figure 4.6). This cut is applied on all events which have more than one track (the main one) observed in the near TPCs.

The previous selection considered only the distance between the start positions of the positive muon candidate and the second highest momentum track. If this distance is too close the event was rejected. We think this cut is too restrictive so we choose to measure, not only the distance between the two starting position in z direction (Δz), but also the ratio (p_{ratio}) between the momentum of the secondary track and the momentum of the candidate track. Theoretically if the track is broken, the momentum ratio is higher than one. Obviously, in an event, we can have more than one secondary track, therefore an event pass the cut if all the secondary tracks respect the cut. The Figure 4.7 shows the distribution of the Δz and p_{ratio}. The analysis of the η parameter shows that the best values for the cut are $p_{ratio} < 0.80$ and $\Delta z > -20mm$. In this way the Upstream veto cut has the following parameters:

$$\begin{aligned} \rho &= 57.7 \pm 0.2\% \\ \epsilon &= 90.2 \pm 0.1\% \\ \eta &= 52.0 \pm 0.2\% \end{aligned} \tag{4.11}$$

4.6.3 Particle identification

For tracks which satisfy the criteria described above, particle identification procedure is applied. In this step we will use, as much as possible, the information that came from various sub-detectors. For the FWD sample we use TPCs, FGD2, Barrel-ECal and DsECal. We divide the PID cut in two phases: **TPC PID** and **FGD2/ECAL PID**.

TPC PID

The procedure of this cut is the same of the previous $\bar{\nu}_\mu$ selection: measured energy deposit in TPC is compared with the expected energy deposit under the assumption of the particle type hypothesis (proton, pion, positron). Based on that information, pulls

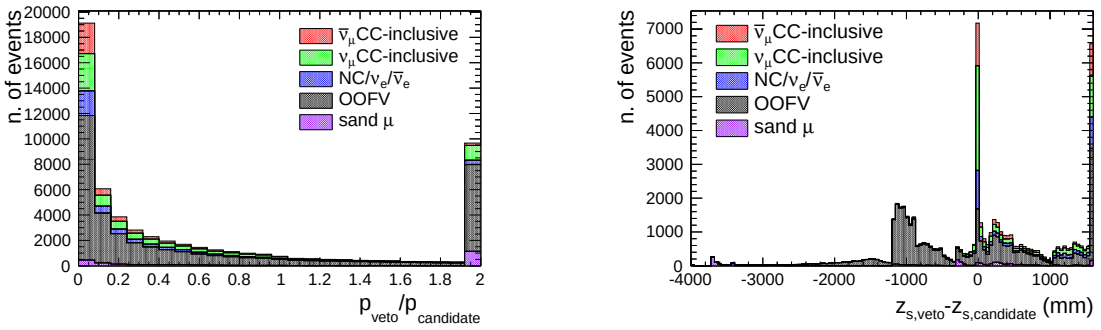

(a) (b)

Figure 4.7: The figure (a) shows the ratio between the momentum of the veto candidate track and the positive muon candidate. The figure (b) shows the distance between the z coordinate of the start of the veto track and the z coordinate of the start of the positive muon candidate, $\Delta z = 0$ indicates that the secondary track starts in the same layer of the main track. The last bin in all plots contains the overflow too. Colours indicate the different topologies of interaction.

and discrimination functions (L_μ and L_{MIP}) are calculated (Figure 4.8).

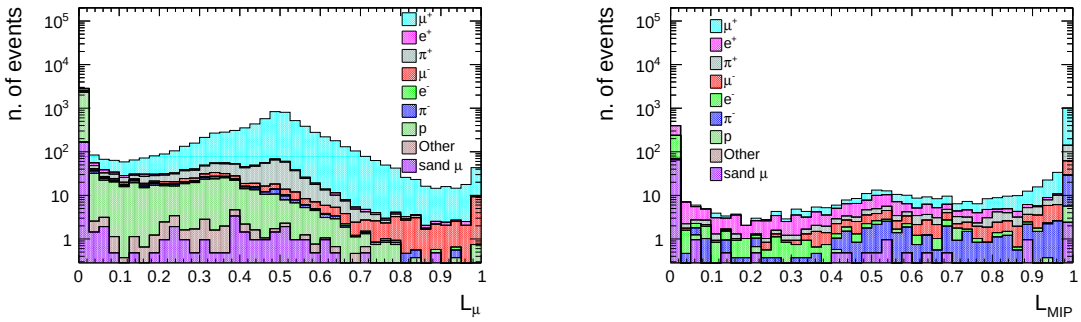

(a) (b)

Figure 4.8: L_μ value for positive muon candidate in FWD selection (left). L_{MIP} value for positive muon candidate when momentum is lower than 500 MeV/c (right). Colours indicate the true particle type selected as positive muon candidate.

The function L_{MIP} is used to separate positron to positive muons that have similar energy loss in TPC at low energy as we can see from Figure 4.9.
So we apply first the cut on the L_μ, and after for all the events with $p < 500\,MeV/c$, we use the cut on the L_{MIP}. The analysis of this cut produces that the best configuration for the TPC cuts is: $L_\mu > 0.07$ and $L_{MIP} > 0.47$. The values of the analysis parameters

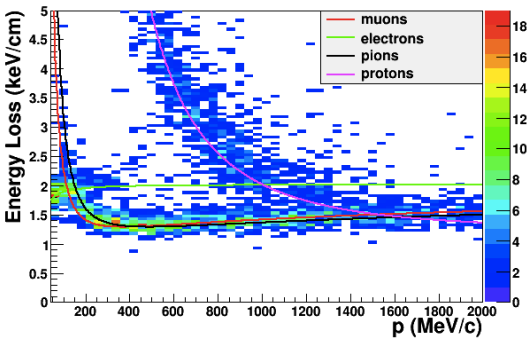

Figure 4.9: Deposit energy, measured (points) and expected (lines), in a TPC for different positive charged particle: positive muon, positron, pion and proton.

with this choice are:

$$\begin{aligned} \rho &= 78.54 \pm 0.15\% \\ \epsilon &= 95.69 \pm 0.08\% \\ \eta &= 75.15 \pm 0.16\% \end{aligned} \tag{4.12}$$

FGD2 PID

FGD2 can be used to distinguish between positive muons and pions (main background of this selection) and protons. The idea is that the behaviour of positive muons and hadron particles is different when they stop in FGD2. Hadron with less than 200 MeV/c are more likely to stop in the wall of the FGD2 than positive muons. So we want to define a FGD2 FV for the stopping particle and observe the momentum of these particles too.

As shown in Figure 4.10, most of the positive muons stopping in the last module of

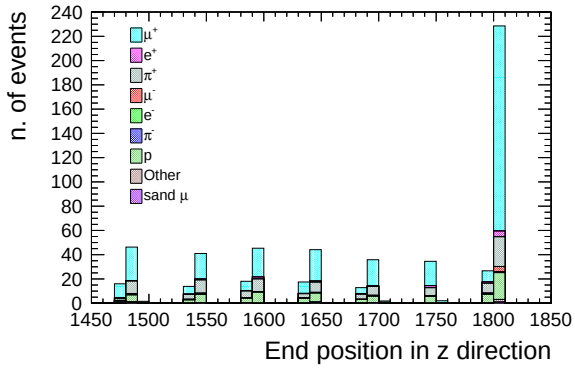

Figure 4.10: End position of the positive muon candidate in z direction that fulfils TPC positive muon PID criteria ends in FGD2 detector. Colours identify the true particle produced in the interaction.

scintillators, so we reject all events where the positive muon candidate stops in FGD2 with $z < 1800$ mm. This cut excludes mainly pion background.
We apply another condition to this cut, in order to reject proton events. We observe the reconstructed momentum (Figure 4.11) of the positive muon candidate which stops in FGD2 and we reject all the events with $p > 800\, MeV/c$.

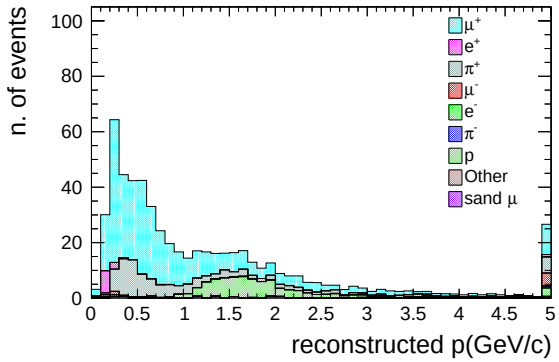

Figure 4.11: Momentum of the positive muon candidate that fulfils TPC positive muon PID criteria and ends in FGD2 detector with $z > 1800$. The last bin contains the all the overflow. Colours identify the true particle produced in the interaction.

ECAL PID

For the events that do not end in FGD2 but go through the ECAL, we apply another cuts based on ECAL PID capability. In Figure 4.12, two different calorimeters are reached by positive muon candidate in the FWD selection: DsECAL and Barrel-ECAL. If the interested detector is the Barrel-ECAL we use the variable *MipEM* (Figure 4.13). The MipEM is a discriminator designed to separate $e^{\pm}$ and γ from $\mu^{\pm}$. This discriminator is formed using the Log Likelihood Ratio method and it is computed considering the ECAL cluster charge distribution and shape. The interested variables to this measurement are:

- *Circularity*: this variables distinguish short-and-fat (shower-like) cluster, typically of $e^{\pm}$ and γ, from long-and-thin (track-like) cluster, typically of $\mu^{\pm}$
- *QMRS*: this is the standard deviation of the hit charges in the cluster. Electromagnetic showers tend to have larger QMRS that MIP-like muons.
- *Total Charge*: the total charge in each ECAL layer is computed. Before the computing of the total charge for layer, the highest and lowest charge hits are removed to reduce the sensitivity to noise or saturated channels.
- *Front Back Ratio*: is a measure of $\frac{dE}{dx}$ along a track. It is defined as the total charge in the back quarter divided by the total charge in the front quarter. It is sensitive to the $\frac{dE}{dx}$ profile of stopping tracks.

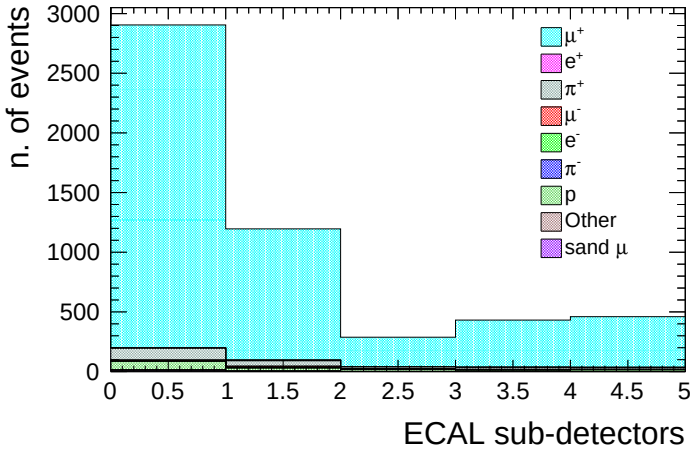

Figure 4.12: ECAL sub-detector that positive muon candidate reaches (0 = Downstream, 1 = Bottom-Barrel, 2 = Top-Barrel, 3 = Left-Barrel, 4 = Right-Barrel). Colours indicate true particle type produced in the interaction.

On the other hand, when the positive muon candidate reaches DsECAL, most of the muons leaves the detector or stops in the first layer. Therefore, requiring that the tracks end within certain DsECAL volume enhances the positive muon contribution (Figure 4.14). In order to reduce the positive muon contribution for track stopping within the DsECAL volume, we use MipEM variable too (Figure 4.15).

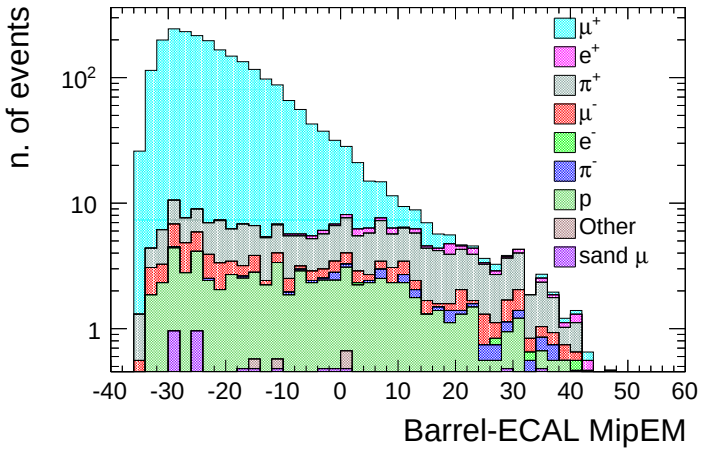

Figure 4.13: MipEM value of the positive muon candidate that fulfils TPC PID criteria and reaches one Barrel-ECAL detector. Colours indicate true particle type produced in the interaction.

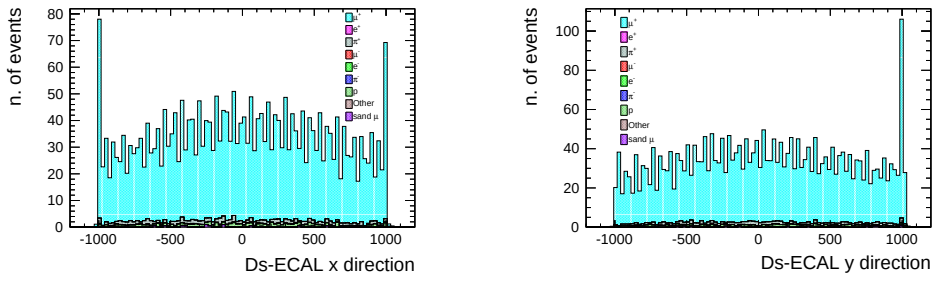

(a) (b)

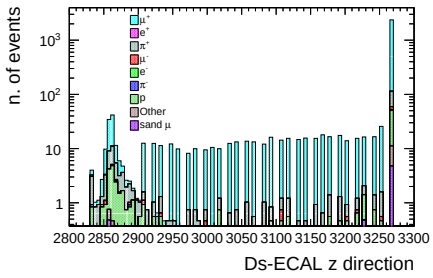

(c)

Figure 4.14: End position of the positive muon candidate that fulfils TPC PID criteria and reaches DsECAL detector. Colours indicate true particle type produced in the interaction. The peaks in (a) are due to edge effects, while the single peak in (b) can be explained by the deviation of the positive particle due the magnetic field of ND280.

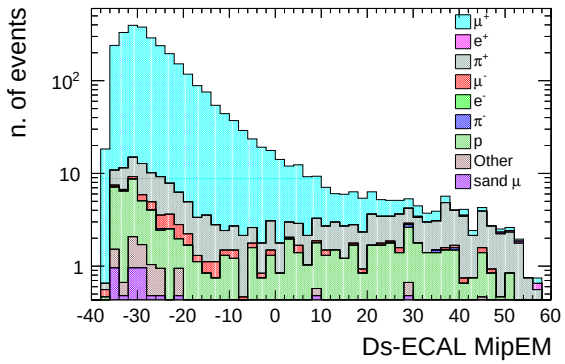

Figure 4.15: MipEM value of the positive muon candidate that fulfils TPC PID criteria and reaches DsECAL detector. Colours indicate true particle type produced in the interaction.

The analysis shows that we have to reject the positive muon candidate which reaches the Barrel-ECAL with Barrel-MipEM ≥ 4.6, or stops in the DsECAL volume, defined by $z_{position} < 2840$, with Ds-MipEM ≥ 12. The analysis parameters for this cut are:

$$\begin{aligned} \rho &= 78.6 \pm 0.2\% \\ \epsilon &= 99.54 \pm 0.03\% \\ \eta &= 78.3 \pm 0.2\% \end{aligned} \tag{4.13}$$

Results of the FWD selection are presented in Figure 4.16, where we show the reconstructed momentum distribution and the $\cos\theta$ distribution when the positive muon candidate fulfilled all FWD selection criteria.

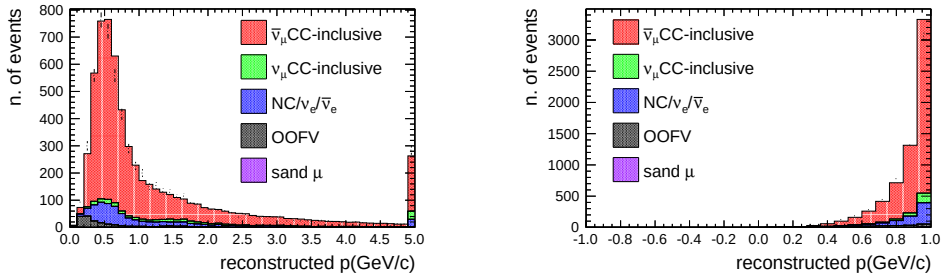

(a) (b)

Figure 4.16: Momentum (a) and cosine of emission angle (b) for the positive muon candidate that fulfils all FWD selection criteria. Colours identify different topologies of interaction and the black points indicate data variables.

4.7 Backward sample

The cuts that we apply to the *Backward* sample (BWD) are very similar to those already described for the FWD sample. There is only one difference, in this case we cannot take information for PID from FGD2 detector and ECAL detector because these sub-detector are not reached by anti-muon candidate.

4.7.1 FGD1 layer cut

In this case the positive muon candidate is the highest momentum positive charged low angle track starting in the FGD1 FV and it must have backward sense. The BWD sample is dominated by OOFV events, as we expected, because this events are charaterized by low energy so the reconstruction of the tracks is more difficult than in the other cases. In order to reject OOFV events we exclude the layers 0-1-26-27-28-29 (Figure 4.17). The values of the analysis parameters are summarized in Table 4.6.

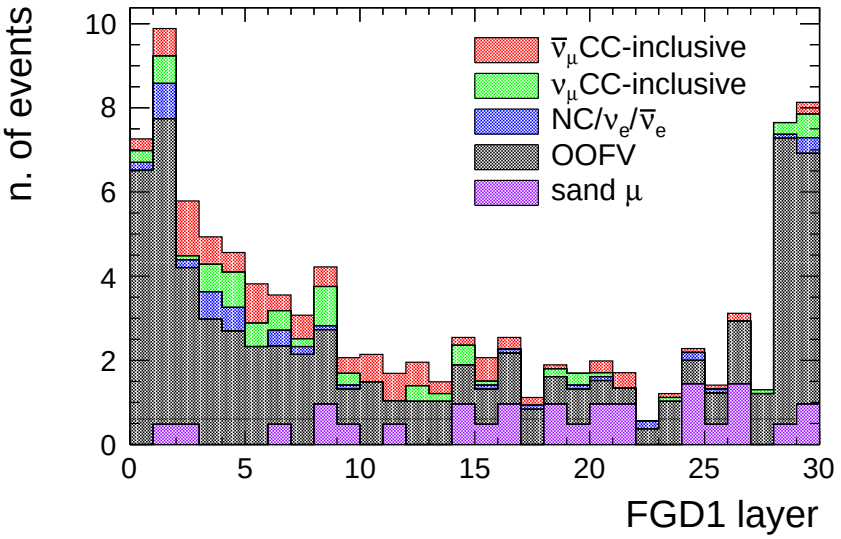

Figure 4.17: Start layer in FGD1 of the positive muon candidate for BWD sample. Colours indicate different topologies of interaction.

Excluded layer	ρ (%)	ϵ (%)	η (%)
0	13.4±1.2	97.4±1.5	13.1±1.2
0-1	14.3±1.3	91.4±2.6	13.1±1.2
0-29	14.4±1.3	94.9±2.0	13.7±1.2
0-1-29	15.5±1.4	88.9±2.9	13.8±1.3
0-28-29	16.0±1.4	94.9±2.0	15.2±1.4
0-1-28-29	17.6±1.6	88.9±2.9	15.7±1.5
27-28-29	15.1±1.3	97.4±1.5	14.7±1.3
26-27-28-29	15.2±1.3	95.7±1.9	14.6±1.3
0-1-27-28-29	18.0±1.6	88.9±2.9	16.0±1.5
0-1-26-27-28-29	18.3±1.6	87.2±3.1	16.0±1.5

Table 4.6: Results of the FGD1 vertex cut analysis for the BWD sample.

4.7.2 Veto cut

In order to further reduce the OOFV component in the BWD sample, we analyze the two variables p_{ratio} and Δz (Figure 4.18).
In this case, if the event in the BWD sample has more than one track in the TPCs, this is almost certainly an OOFV event. Thus, only those events that do not have secondary

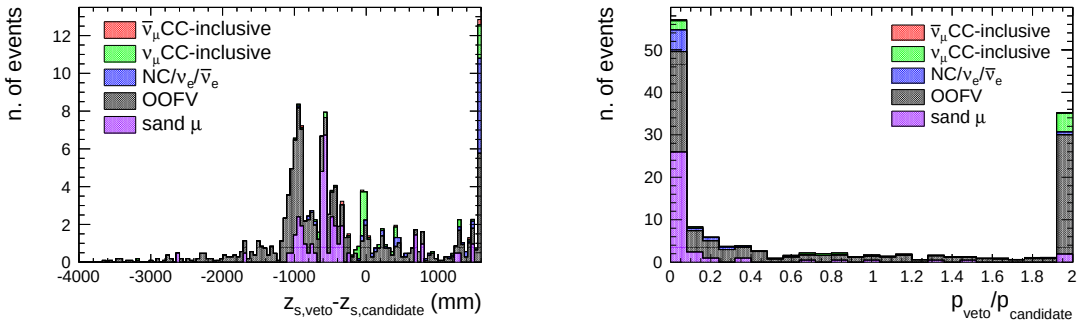

Figure 4.18: Distribution of the variables Δz (left) and p_{ratio} (right) for the events with secondary tracks in BWD sample. The last bin contains all the overflow. Colours identify different topologies interaction.

tracks in the TPCs exceed the veto cut. The analysis parameters for this cut are:

$$\begin{aligned} \rho &= 41.3 \pm 3.3\% \\ \epsilon &= 91.3 \pm 2.8\% \\ \eta &= 37.7 \pm 3.2\% \end{aligned} \tag{4.14}$$

4.7.3 TPC PID

In this case we can only perform the TPC particle identification, so we use the functions L_μ and L_{MIP} to identify as many positive muons as possible. The parameters analysis shows as best cuts value: $L_\mu > 0.01$ and $L_{MIP} > 0.5$. The Table 4.7 summarized the parameters analysis.

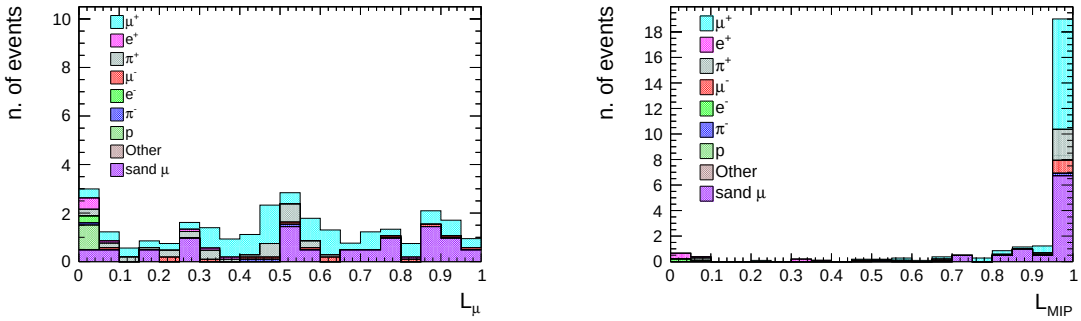

Figure 4.19: L_μ value for positive muon candidate in BWD selection (left). L_{MIP} value for positive muon candidate when momentum is lower than 500 MeV/c (right). Colours indicate the true particle type selected as positive muon candidate.

In the end we show the comparisons between data and Monte Carlo in the Figure 4.20, where we see the momentum and the $\cos\theta$ distributions when the positive muon candidate

L_μ	$\rho(\%)$	$\epsilon(\%)$	$\eta(\%)$
> 0.01	44.9 ± 3.5	98.9 ± 1.1	44.4 ± 3.5
> 0.02	45.0 ± 3.5	97.8 ± 1.5	44.1 ± 3.5
> 0.03	45.3 ± 3.5	97.8 ± 1.5	44.3 ± 3.5
> 0.04	45.4 ± 3.5	96.8 ± 1.8	44.0 ± 3.5
> 0.05	45.2 ± 3.5	95.7 ± 2.1	43.2 ± 3.5
> 0.06	45.0 ± 3.6	92.5 ± 2.7	41.6 ± 3.6
> 0.07	45.5 ± 3.6	92.5 ± 3.5	42.0 ± 3.6
> 0.08	45.7 ± 3.6	92.5 ± 3.5	42.3 ± 3.6

(a)

L_{MIP}	$\rho(\%)$	$\epsilon(\%)$	$\eta(\%)$
> 0.3	45.5 ± 3.5	98.9 ± 1.1	45.0 ± 3.6
> 0.4	46.2 ± 3.6	98.9 ± 1.1	45.7 ± 3.6
> 0.5	45.5 ± 3.5	98.9 ± 1.1	46.2 ± 3.7
> 0.6	46.9 ± 3.6	97.8 ± 1.5	45.9 ± 3.8
> 0.7	46.5 ± 3.6	94.6 ± 2.4	44.0 ± 3.7
> 0.8	45.6 ± 3.7	91.3 ± 2.9	41.7 ± 3.6

(b)

Table 4.7: Results of the parameters for the two step of the TPC PID for BWD sample.

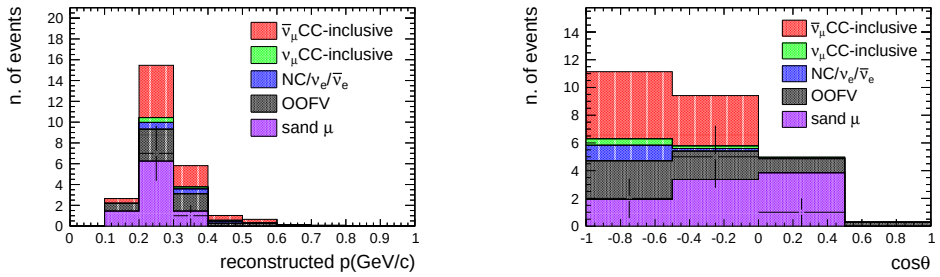

(a) (b)

Figure 4.20: Momentum (a) and cosine of emission angle (b) for the positive muon candidate when all BWD criteria are fulfilled. Colours identify different topologies of interaction and the black points indicate data variables.

fulfilled the BWD selection criteria.
The difference between Monte Carlo and Data can be explained by the little statistics of the sample and by the fact that in the backward-going direction the Monte Carlo has a reconstructed issue.

4.8 High angle forward and backward sample

In this section, we will report the details of the selection of two sub-samples, High Angle Forward (HAFWD) and High Angle Backward (HABWD), at the same time as the steps performed are the same. It is really important to understand which events constitute these samples: high angle tracks are defined as tracks starting in FGD1 FV, they have less than 19 hits in TPCs, and they stop in SMRD or Barrel-ECAL. We need this last requirement because for these tracks the momentum is measured only by their range, since such tracks do not pass through TPCs.

4.8.1 FGD1 layer cut

In order to reduce the OOFV contamination in the samples, we analyse the distribution of the vertex of the positive muon candidate in each layer of FGD1 (Figure 4.21). The

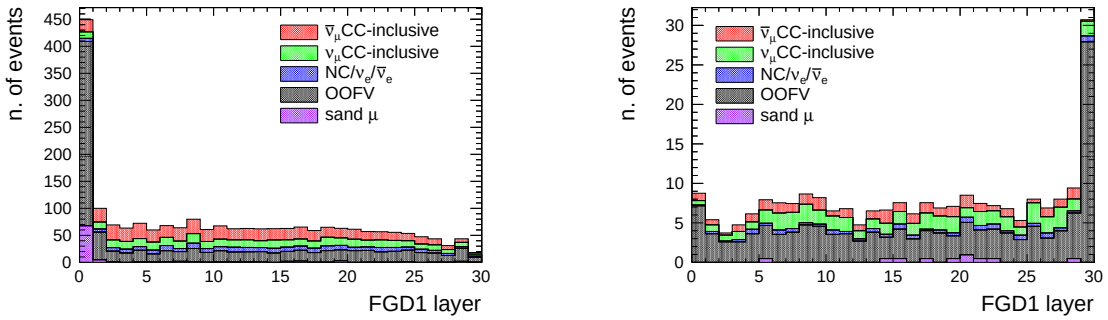

(a) (b)

Figure 4.21: The figures show the reconstructed starting vertex in FGD1 for the HAFWD sample (a) and HABWD sample (b). Colours identify different topologies of interaction.

optimization of this cut gives as result:

- for HAFWD selection are rejected events with vertex in the first or last two layers;
- for HABWD selection are rejected events with vertex in the first or last layer;

4.8.2 Upstream veto cut

The concept behind veto cut is the same as the one introduced in the FWD and BWD selections. The variables p_{ratio} and Δz are optimised for each sample independently (see Figure 4.22 and Figure 4.23).

The results of the analysis of these cuts for the HAFWD selection are $p_{ratio} < 1$ and $\Delta z >$ -80 mm, for the HABWD selection are $p_{ratio} <$ 0.80 and $\Delta z >$ -240 mm. The parameters values for the two selection are summarized in the Table 4.9.

Excluded layers	$\rho(\%)$	$\epsilon(\%)$	$\eta(\%)$
0	32.3 ± 0.3	96.1 ± 0.2	31.0 ± 0.3
0-1	32.6 ± 0.4	91.7 ± 0.4	29.9 ± 0.4
0-29	32.5 ± 0.3	95.6 ± 0.3	31.0 ± 0.3
0-1-29	32.8 ± 0.4	91.2 ± 0.4	29.9 ± 0.4
0-28-29	32.9 ± 0.4	94.4 ± 0.3	31.1 ± 0.4
0-1-28-29	33.2 ± 0.4	90.0 ± 0.4	29.9 ± 0.4

(a)

Excluded layers	$\rho(\%)$	$\epsilon(\%)$	$\eta(\%)$
0	13.3 ± 0.7	97.3 ± 0.9	13.1 ± 0.7
0-1	13.5 ± 0.7	95.2 ± 1.2	12.8 ± 0.7
0-29	15.5 ± 0.8	96.7 ± 1.0	15.0 ± 0.8
0-1-29	15.6 ± 0.8	94.6 ± 1.3	14.8 ± 0.8
0-28-29	15.5 ± 0.8	92.1 ± 1.5	14.3 ± 0.8
0-1-28-29	15.6 ± 0.8	90.0 ± 1.7	14.1 ± 0.8
0-1-2-29	15.8 ± 0.8	93.6 ± 1.3	14.8 ± 0.8

(b)

Table 4.8: Results of the parameters for the FGD1 vertex cut for the HAFWD (a) and HABWD (b).

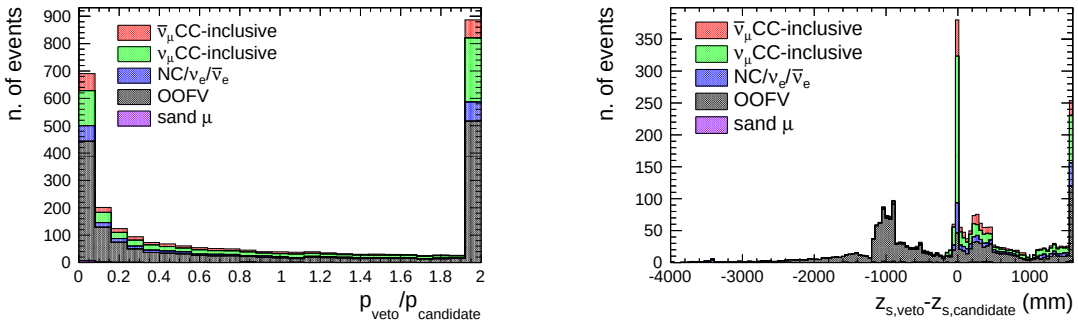

(a) (b)

Figure 4.22: Ratio between the momentum of the veto track and the positive muon candidate track in HAFWD selection (a). Distance between start position of the veto track and the positive muon candidate track in HAFWD selection (b). The last bins contains all the overflow. Colours identify the different topologies of interaction.

4.8.3 Particle identification

The analysis of the particle identification for the two high angle samples uses the information taken by the Barrel ECal and the SMRD. First we study the events which stop

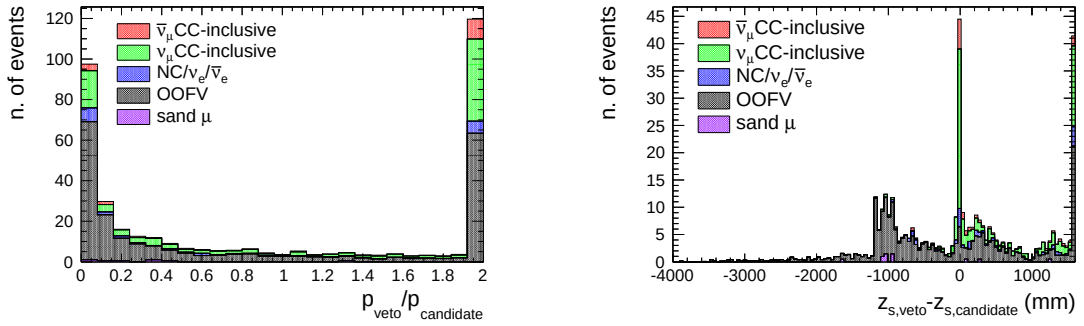

(a) (b)

Figure 4.23: Ratio between the momentum of the veto track and the positive muon candidate track in HABWD selection (a). Distance between start position of the veto track and the positive muon candidate track in HABWD selection (b). The last bins contains all the overflow. Colours identify the different topologies of interaction.

Sub-sample	$\rho(\%)$	$\epsilon(\%)$	$\eta(\%)$
High Angle Forward	50.3 ± 0.5	86.5 ± 0.4	43.5 ± 0.5
High Angle Backward	22.8 ± 1.3	74.0 ± 2.5	16.9 ± 1.1

Table 4.9: The parameters values after the veto cut for the two high angle samples.

in the SMRD (Figure 4.24). If we measure the purity of the group of event which stops in the SMRD we found for HAFWD $\rho = 57.1 \pm 1.0\%$, and for HABWD $\rho = 5.5 \pm 2.4\%$. So we assume: if a positive muon candidate track stops in the SMRD for HAFWD, it is a good $\bar{\nu}_\mu$ CC event. This is the contrary for HABWD selection. If the main track

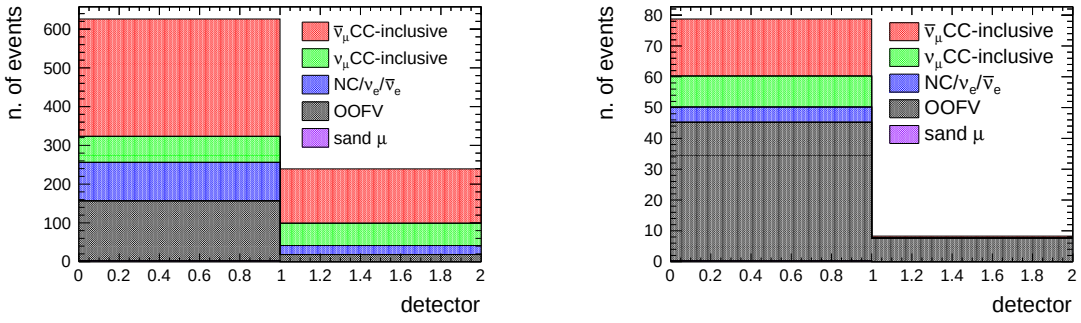

(a) (b)

Figure 4.24: Sub-detector in which positive muon candidate stops in HAWD (a) and HABWD (b) selections (0 = BarrelECal, 1=SMRD). Colours identify true topologies of interaction.

does not stop in the SMRD but in Barrel-ECal we use two variables to make the particle identification: MipEM and the ratio between the track length and the deposit electromagnetic energy in ECAL. The distribution of these discriminators for the HAFWD and HABWD selections are represented in Figure 4.25. The analysis gives as best results for these variables: Barrel-MipEM < 5 and Barrel-Length/EMEnergy between 0.75 and 2.3 for HAFWD selection, and Barrel-MipEM < 6 and Barrel-Length/EMEnergy between 0.65 and 2.3 for HABWD selection.

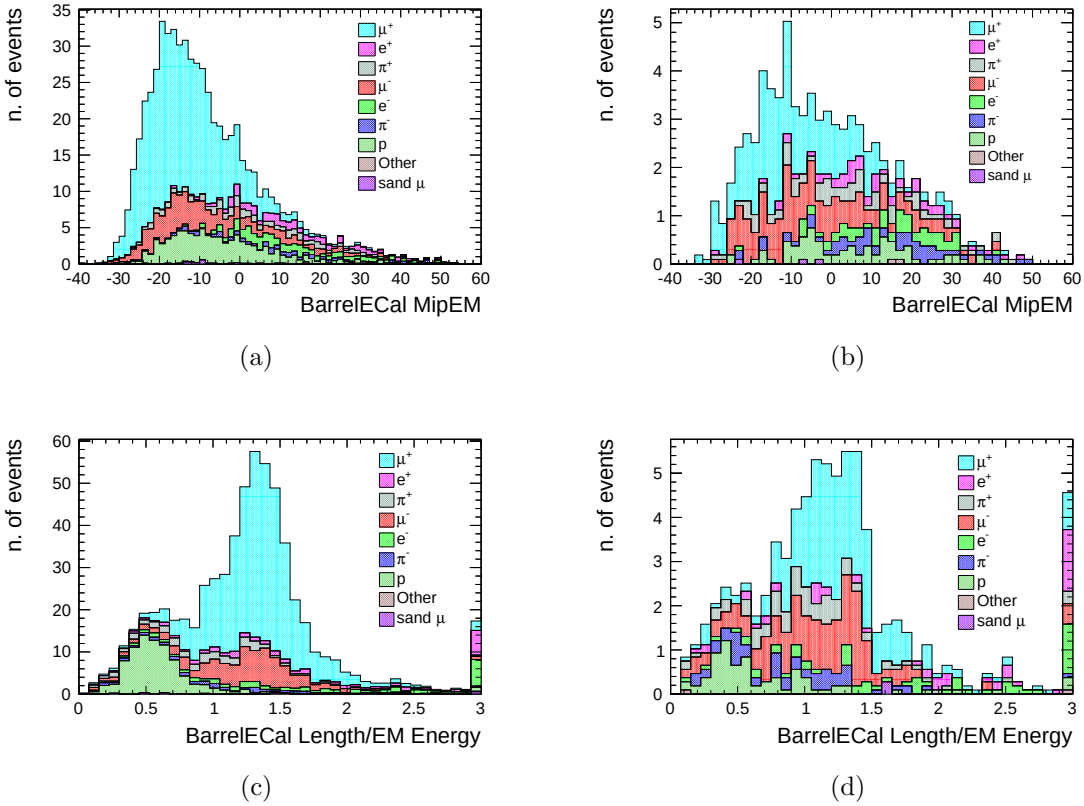

Figure 4.25: Distribution of the Barrel-MipEM discriminator for the HAFWD (a) and HABWD (b) selection. Distribution of the Barrel-Length/EMEnergy discriminator for the HAFWD (c) and HABWD (d) selection. The last bins contains all the overflow. Colours identify different true particle of the main track and the black point indicate the data variables.

In Figures 4.26 and 4.27 the distribution of the reconstructed momentum and of the $\cos\theta$ for HAFWD and HABWD respectively are shown. The purity of HAFWD sample is $\rho = 62.0 \pm 0.6\%$, and for HABWD is $\rho = 38.1 \pm 2.2\%$. The inconsistencies between Data and Monte Carlo can be traced back to the difficulty of recontructing the momentum and the $\cos\theta$ of the positive muon candidate.

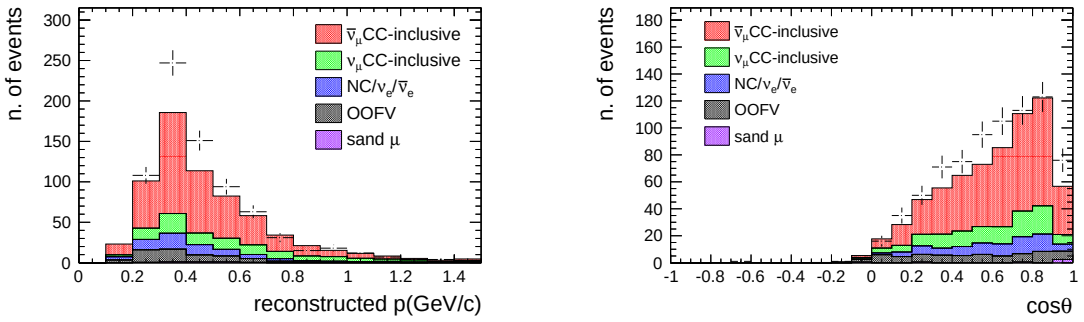

(a) (b)

Figure 4.26: Distribution of the reconstructed momentum (a) and of the $\cos\theta$ (b) of the HAFWD events which pass all selection criteria. Colours identify different topologies of interaction and the black point indicate the data variables.

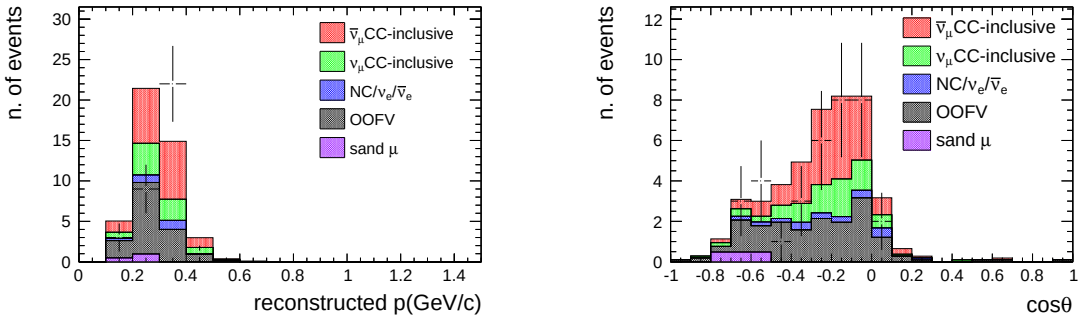

(a) (b)

Figure 4.27: Distribution of the reconstructed momentum (a) and of the $\cos\theta$ (b) of the HABWD events which pass all selection criteria. Colours identify different topologies of interaction and the black point indicate the data variables.

Conclusion and future outlook

At the end of the selection, we gather all the events selected by the four sub-samples (FWD, BWD, HAFWD, HABWD). The final distributions of the reconstructed momentum and of the cosine of the scattering angle w.r.t. beam direction of the positive muon are shown in Figure 4.28. As can be seen, we found a sample of $\bar{\nu}_\mu$ CC interactions with

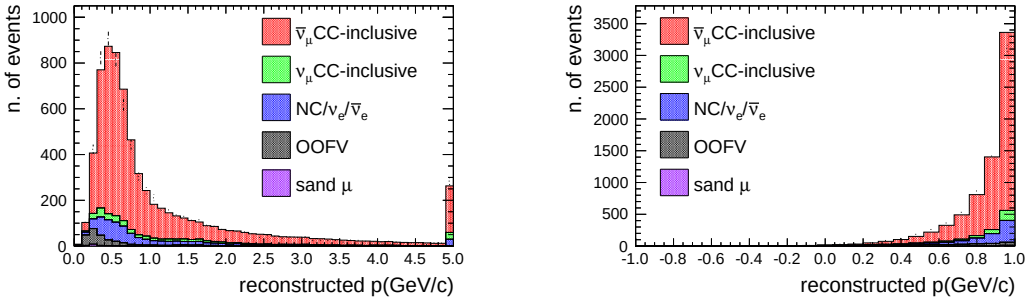

(a) (b)

Figure 4.28: Distribution of the reconstructed momentum (a) and of the $\cos\theta$ (b) of the $\bar{\nu}_\mu\, CC$ sample after the selection. Colours identify different topologies of interaction and the black point indicate the data variables.

a purity and efficiency of 80.1 % and 61.9 % respectively. Where the efficiency is defined as the ratio between the number of true events that fulfill the selection and the total number of true event generated. The composition of final sample is summarized in Table 4.10.

A good result of our selection is the purity of the FWD sample as a function of positive muon ($\rho_{par} = 95.0\%$). In Table 4.11 we summarize the composition of the four sub-samples as a function of the true particle produced in the interaction. In FWD and BWD selections the dominant background is associated with positive pions which are misidentified as μ^+ in TPC. In the BWD this contribution is more accentuated because, as we saw in the previous chapter, the backward-going track events are characterised by low energy, so the expected deposit energy in TPC between μ^+ and π^+ is very similar. In the high angle selections the main background is composed by μ^-. In this case the problem is linked to the reconstruction of the curvature of the track, which determine the charge

	Fraction(%)
True reaction	Sample
$\bar{\nu}_\mu$CC-inclusive	80.1
ν_μCC-inclusive	5.2
NC, ν_e,$\bar{\nu}_e$	10.6
Out of FGD1 FV	4.0
sand μ	0.1

Table 4.10: Composition of the final sample.

True particle	FWD (%)	BWD (%)	HAFWD (%)	HABWD (%)
μ^+	95.0	62.6	73.1	54.6
μ^-	0.5	7.6	19.6	27.0
e^+	0.1	0.5	0.7	1.5
e^-	0	0	0.9	1.5
π^+	2.4	18.2	2.6	8.6
π^-	0	1.5	1.1	3.7
proton	1.8	0	1.9	2.4
other	0.2	0	0	0
sand μ	0	9.6	0.1	0.7

Table 4.11: Positive muon candidate composition according to particle type.

of track. In Table 4.12 we can see the composition of the four sub-samples as a function of the true event interaction. The main background is the OOFV for the backward-going tracks. This is related to the difficulty to reconstruct the charge and the sense of the track, that heavily depend on the possibility the have a Time of Flight between FGD1-P0D (really difficult because the upstream layer, w.r.t. beam direction, is made of lead and the backward-going tracks have very low energy) or FGD1-ECAL. In order to improve the high angle and backward selection and reduce the main backgrounds, the Collaboration propose an upgrade to ND280. In this proposal a new tracker, consisting of a 2 ton horizontal plastic scintillator target sandwiched between two new horizontal TPCs, will replace the P0D detector as shown in Figure 4.29. This tracker would be

True particle	FWD (%)	BWD (%)	HAFWD (%)	HABWD (%)
$\bar{\nu}_\mu$CC-inclusive	85.4	46.0	63.1	38.5
ν_μCC-inclusive	3.1	4.0	16.9	18.8
NC, ν_e,$\bar{\nu}_e$	10.0	7.1	10.5	5.4
OOFV	1.5	33.3	9.4	36.7
sand μ	0	9.6	0.1	0.6

Table 4.12: Positive muon candidate composition according to the interaction type.

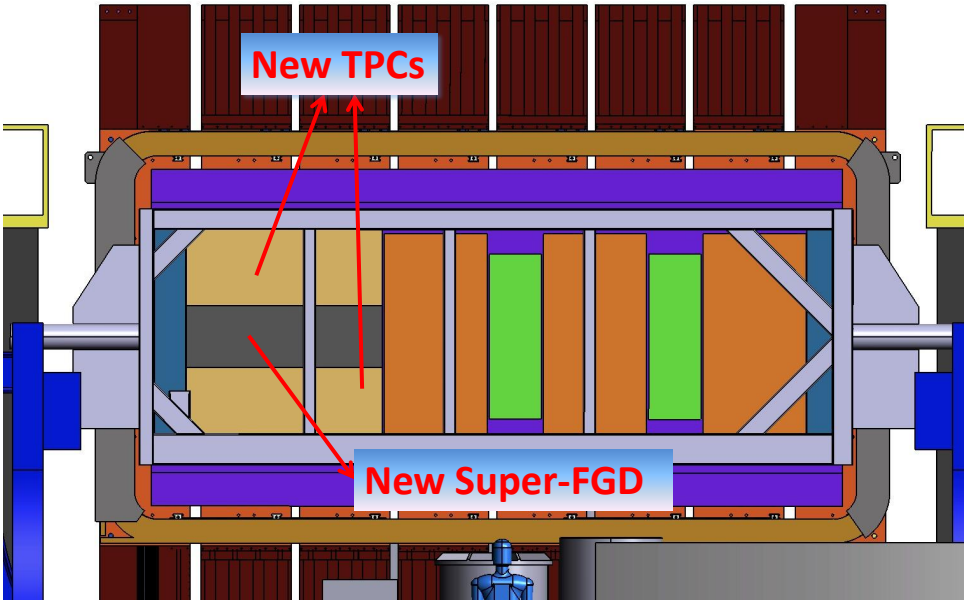

Figure 4.29: A schematic view of the ND280 upgrade.

surrounded by Time-of-Flight detector to measure the direction of the tracks, in this way the detector improve the capability of reconstructed the charge and the sense of track, even at high angle [23].

Bibliography

[1] K. Abe et al. "Measurements of neutrino oscillation in appearance and disappearance channels by the T2K experiment with 6.6×10^{20} protons on target". In: *Phys. Rev.* D91.7 (2015), p. 072010. DOI: 10.1103/PhysRevD.91.072010. arXiv: 1502.01550 [hep-ex].

[2] K. Abe et al. "Search for CP violation in Neutrino and Antineutrino Oscillations by the T2K experiment with 2.2×10^{21} protons on target". In: (2018). arXiv: 1807.07891 [hep-ex].

[3] K. Abe et al. "The T2K Experiment". In: *Nucl. Instrum. Meth.* A659 (2011), pp. 106–135. DOI: 10.1016/j.nima.2011.06.067. arXiv: 1106.1238 [physics.ins-det].

[4] Y. Abe et al. "Measurement of θ_{13} in Double Chooz using neutron captures on hydrogen with novel background rejection techniques". In: *JHEP* 01 (2016), p. 163. DOI: 10.1007/JHEP01(2016)163. arXiv: 1510.08937 [hep-ex].

[5] P. Adamson et al. "Combined analysis of ν_μ disappearance and $\nu_\mu \to \nu_e$ appearance in MINOS using accelerator and atmospheric neutrinos". In: *Phys. Rev. Lett.* 112 (2014), p. 191801. DOI: 10.1103/PhysRevLett.112.191801. arXiv: 1403.0867 [hep-ex].

[6] N. Agafonova et al. "Final Results of the OPERA Experiment on ν_τ Appearance in the CNGS Neutrino Beam". In: *Phys. Rev. Lett.* 120.21 (2018). [Erratum: Phys. Rev. Lett.121,no.13,139901(2018)], p. 211801. DOI: 10.1103/PhysRevLett.121.139901,10.1103/PhysRevLett.120.211801. arXiv: 1804.04912 [hep-ex].

[7] A. Aguilar-Arevalo et al. "Evidence for neutrino oscillations from the observation of anti-neutrino(electron) appearance in a anti-neutrino(muon) beam". In: *Phys. Rev.* D64 (2001), p. 112007. DOI: 10.1103/PhysRevD.64.112007. arXiv: hep-ex/0104049 [hep-ex].

[8] A. A. Aguilar-Arevalo et al. "First Measurement of the Muon Neutrino Charged Current Quasielastic Double Differential Cross Section". In: *Phys. Rev.* D81 (2010), p. 092005. DOI: 10.1103/PhysRevD.81.092005. arXiv: 1002.2680 [hep-ex].

[9] M. H. Ahn et al. "Measurement of Neutrino Oscillation by the K2K Experiment". In: *Phys. Rev.* D74 (2006), p. 072003. DOI: 10.1103/PhysRevD.74.072003. arXiv: hep-ex/0606032 [hep-ex].

[10] F. P. An et al. "New Measurement of Antineutrino Oscillation with the Full Detector Configuration at Daya Bay". In: *Phys. Rev. Lett.* 115.11 (2015), p. 111802. DOI: 10.1103/PhysRevLett.115.111802. arXiv: 1505.03456 [hep-ex].

[11] D. Beavis et al. "Long Baseline Neutrino Oscillation Experiment at the AGS Approved by the HENPAC as AGS Experiment 889". In: (1995). DOI: 10.2172/52878.

[12] Veronique Bernard, Latifa Elouadrhiri, and Ulf-G. Meissner. "Axial structure of the nucleon: Topical Review". In: *J. Phys.* G28 (2002), R1–R35. DOI: 10.1088/0954-3899/28/1/201. arXiv: hep-ph/0107088 [hep-ph].

[13] J. H. Choi et al. "Observation of Energy and Baseline Dependent Reactor Antineutrino Disappearance in the RENO Experiment". In: *Phys. Rev. Lett.* 116.21 (2016), p. 211801. DOI: 10.1103/PhysRevLett.116.211801. arXiv: 1511.05849 [hep-ex].

[14] L. De Braeckeleer. "Neutrino physics with the KamLAND detector". In: *Nucl. Phys. Proc. Suppl.* 87 (2000). [,312(2000)], pp. 312–314. DOI: 10.1016/S0920-5632(00)00689-7.

[15] A.L. Fetter and J.D. Walecka. *Quantum theory of many-particle systems*. International series in pure and applied physics. McGraw-Hill, 1971. URL: https://books.google.co.jp/books?id=tofKnQEACAAJ.

[16] J. A. Formaggio and G. P. Zeller. "From eV to EeV: Neutrino Cross Sections Across Energy Scales". In: *Rev. Mod. Phys.* 84 (2012), pp. 1307–1341. DOI: 10.1103/RevModPhys.84.1307. arXiv: 1305.7513 [hep-ex].

[17] Y. Fukuda et al. "Atmospheric muon-neutrino / electron-neutrino ratio in the multiGeV energy range". In: *Phys. Lett.* B335 (1994), pp. 237–245. DOI: 10.1016/0370-2693(94)91420-6.

[18] Reddy Pratap Gandrajula and Micah Groh. "Systematic Uncertainties and Cross-Checks for the NOvA Joint ν_μ+ν_e Analysis". In: *28th International Conference on Neutrino Physics and Astrophysics (Neutrino 2018) Heidelberg, Germany, June 4-9, 2018*. 2018. arXiv: 1808.10760 [hep-ex]. URL: https://doi.org/10.5281/zenodo.1292418.

[19] Johnathon R. Jordan et al. "Severe Constraints on New Physics Explanations of the MiniBooNE Excess". In: (2018). arXiv: 1810.07185 [hep-ph].

[20] Syunsuke Kasuga. "Observation of a Small Muon-neutrino / Electron-neutrino Ratio of Atmospheric Neutrinos in Super-Kamiokande by the Method of Particle Identification". PhD thesis. Tokyo U., 1998. URL: http://www-sk.icrr.u-tokyo.ac.jp/sk/pub/index.html#dthesis.

[21] Konstantin S. Kuzmin, Vladimir V. Lyubushkin, and Vadim A. Naumov. "Quasielastic axial-vector mass from experiments on neutrino-nucleus scattering". In: *Eur. Phys. J.* C54 (2008), pp. 517–538. DOI: 10.1140/epjc/s10052-008-0582-x. arXiv: 0712.4384 [hep-ph].

[22] Luis Labarga. "The SuperK-gadolinium project". In: *PoS* EPS-HEP2017 (2018), p. 118. DOI: 10.22323/1.314.0118.

[23] Mathieu Lamoureux. "Upgrade of the T2K near detector ND280: effect on oscillation and cross-section analyses". In: *PoS* NuFact2017 (2018), p. 056. DOI: 10.22323/1.295.0056. arXiv: 1803.02645 [physics.ins-det].

[24] Vladimir Lyubushkin. "A Study of Quasi-Elastic Muon (Anti)Neutrino Scattering in the NOMAD Experiment". In: *AIP Conf. Proc.* 1189 (2009), pp. 157–162. DOI: 10.1063/1.3274147.

[25] M. Martini et al. "A Unified approach for nucleon knock-out, coherent and incoherent pion production in neutrino interactions with nuclei". In: *Phys. Rev.* C80 (2009), p. 065501. DOI: 10.1103/PhysRevC.80.065501. arXiv: 0910.2622 [nucl-th].

[26] C. Patrignani et al. "Review of Particle Physics". In: *Chin. Phys.* C40.10 (2016), p. 100001. DOI: 10.1088/1674-1137/40/10/100001.

[27] T. Patzak. "First direct observation of the tau-neutrino". In: *Europhys. News* 32 (2001), pp. 56–57. DOI: 10.1051/epn:2001205.

[28] Dieter Rein and Lalit M. Sehgal. "Neutrino Excitation of Baryon Resonances and Single Pion Production". In: *Annals Phys.* 133 (1981), pp. 79–153. DOI: 10.1016/0003-4916(81)90242-6.

[29] Ciro Riccio. "Measurement of the antineutrino flux and cross section at the near detector of the T2K experiment". PhD thesis. Università degli Studi di Napoli "Federico II", Universite Paris-Saclay, 2018.

[30] M. Tanabashi et al. "Review of Particle Physics". In: *Phys. Rev.* D98.3 (2018), p. 030001. DOI: 10.1103/PhysRevD.98.030001.

[31] A.W. Thomas and W. Weise. *The Structure of the Nucleon*. Wiley, 2001. ISBN: 9783527402977. URL: https://books.google.it/books?id=ZqAsAAAAYAAJ.